PALEOCEANOGRAPHY, VOL. ???, XXXX, DOI:10.1029/,

How much did Glacial North Atlantic Water shoal?

Geoffrey Gebbie

Department of Physical Oceanography,

Woods Hole Oceanographic Institution,

Woods Hole, Massachusetts, USA

G. Gebbie, Department of Physical Oceanography, Woods Hole Oceanographic Institution, MS #29, Woods Hole, MA 02543, USA. (ggebbie@whoi.edu),

Observations of $\delta^{13}C$ and Cd/Ca from benthic foraminifera have been interpreted to reflect a shoaling of northern source waters by about 1000 meters during the Last Glacial Maximum, with the degree of shoaling being significant enough for the water mass to be renamed Glacial North Atlantic Intermediate Water. These nutrient tracers, however, may not solely reflect changes in water mass distributions. To quantify the distribution of Glacial North Atlantic Water, we perform a glacial water-mass decomposition where the sparsity of data, geometrical constraints, and nonconservative tracer effects are taken into account, and the extrapolation for the unknown water-mass endmembers is guided by the modern-day circulation. Under the assumption that the glacial sources of remineralized material are similar to the modern-day, we find a steady solution consistent with 241 $\delta^{13}C$, 87 Cd/Ca, and 174 $\delta^{18}O$ observations and their respective uncertainties. The water-mass decomposition indicates that the core of Glacial North Atlantic Water shoals and southern source water extends in greater quantities into the abyssal North Atlantic, as previously inferred. The depth of the deep northern-southern water mass interface and the volume of North Atlantic Water, however, are not grossly different from the modern-day. Under this scenario, the vertical structure of glacial $\delta^{13}C$ and Cd/Ca is primarily due to the greater accumulation of nutrients in lower North Atlantic Water, which may be a signal of the hoarding of excess carbon from the atmosphere by the glacial Atlantic.

1. Introduction

The modern-day Atlantic Ocean below 1500 meters depth is vertically homogeneous with high $\delta^{13}C$ (i.e., carbon-13 to carbon-12 isotope ratio) values indicative of North Atlantic Deep Water (NADW), but this feature was replaced by a vertical gradient with lower-$\delta^{13}C$ waters during the Last Glacial Maximum [LGM, e.g., *Duplessy et al.*, 1988; *Curry et al.*, 1988; *Curry and Oppo*, 2005]. The glacial water-mass interface was inferred to shoal to less than 3,300 meters depth [*Streeter and Shackleton*, 1979], to 2,700 meters depth based on the sharp vertical gradient in South Atlantic $\delta^{13}C$ [*Curry and Lohmann*, 1982], and between 2,000 and 2,500 meters depth in the North Atlantic [*Oppo and Lehman*, 1993], corresponding to about 1,000 meters of shoaling relative to the modern-day. The depths of the sharpest vertical gradients in $\delta^{18}O$ and $\delta^{13}C$ coincide, further suggesting a water-mass interface [e.g., *Lund et al.*, 2011]. The large-scale vertical $\delta^{13}C$ gradient corresponds to a nutrient gradient as recorded in the Cd/Ca ratio of benthic foraminifera [e.g., *Boyle and Keigwin*, 1982]. Atlantic-wide compilations of more than 150 $\delta^{13}C$ observations [e.g., *Duplessy et al.*, 1988; *Curry and Oppo*, 2005] and over 70 Cd/Ca observations [*Marchitto and Broecker*, 2006] indicate that waters with low $\delta^{13}C$ ($< 0.6‰$) and high Cadmium (> 0.4nmol/kg) values reside as shallow as 2,500 meters depth in the North Atlantic. The LGM observations have been interpreted as a robust signal of a water-mass divide [e.g., *Lynch-Stieglitz et al.*, 2007], and have led to the definition of a distinct water mass, Glacial North Atlantic Intermediate Water [GNAIW, *Boyle and Keigwin*, 1987; *Duplessy et al.*, 1988].

Ocean circulation models that include biogeochemical processes have simulated glacial configurations with a shoaled distribution of North Atlantic Water [e.g., *Butzin et al.*, 2005; *Tagli-*

abue et al., 2009; *Hesse et al.*, 2011], but the Paleoclimate Model Intercomparison Project found that only about half of the models had a shoaled North Atlantic overturning cell, and that an equal number did not [*Weber et al.*, 2007]. These models generally do not reproduce the paleo-observations within their uncertainty in all regions simultaneously, which partially explains the range of physical solutions. Another interpretational difficulty is due to the nature of the paleo-observations themselves. For example, it is unclear to what extent δ^{13}C gradients reflect changes in the physical source of water versus the accumulation of nutrients [e.g., *Johnson*, 1982]. Biologically-derived remineralization is concentrated in the upper ocean during modern times [e.g., *Martin et al.*, 1987; *Boyd and Trull*, 2007], giving promise that deep δ^{13}C is a nearly conservative tracer [e.g., *Oppo and Fairbanks*, 1987], but some nonconservative effects in δ^{13}C are expected due to remineralization [e.g., *Lynch-Stieglitz*, 2003, and references therein] and have been noted in observations [e.g., *Curry and Lohmann*, 1982]. Even if remineralization rates are highest in the upper ocean, the δ^{13}C distribution depends upon the flow rate and path history, and thus nonconservative effects may accumulate in the relatively sluggish deep ocean. A second major interpretational difficulty is the unknown source values (or endmembers) of southern and northern source waters, which are uncertain due to the lack of observations especially in the Southern Ocean [e.g., *Legrand and Wunsch*, 1995]. These endmembers are critical for quantifying water-mass proportions if inverting a linear mixing model [e.g., *Tomczak*, 1981].

The simultaneous analysis of multiple tracers has aided in the interpretation of the paleodata. For example, δ^{13}C and Cd/Ca can be combined into a nearly conservative tracer that is not subject to the errors in assuming δ^{13}C is conservative [i.e., the air-sea component of δ^{13}C, denoted $\delta^{13}C_{as}$, *Broecker and Maier-Reimer*, 1992; *Lynch-Stieglitz and Fairbanks*, 1994].

This derived tracer shows similarities to δ^{13}C and Cd, with an apparent trend as a function of depth, but $\delta^{13}C_{as}$ is derived from two sparse and uncertain quantities and is not as well determined as δ^{13}C alone. The comparison of δ^{13}C to $\delta^{18}O_c$ (the oxygen-18 to oxygen-16 ratio in foraminiferal calcite) permits a check on δ^{13}C conservation [e.g., *Lund et al.*, 2011], because $\delta^{18}O_c$ is a conservative tracer in the ocean interior aside from pressure heating effects. Furthermore, $\delta^{18}O_c$ is generally stratified due to its similarity to density [e.g., *Lynch-Stieglitz et al.*, 1999], and thus represents a geometrical marker of the spreading direction of waters [*Curry and Oppo*, 2005]. To use the additional information present in Atlantic-wide compilations, however, uncertainties in the deep ocean $\delta^{18}O_c$ due to interlaboratory offsets and differing measurement techniques [e.g., *Ostermann and Curry*, 2000; *Hodell et al.*, 2003] must be overcome. Multiple tracer analysis has also helped estimate uncertain endmembers, where mixing lines in property-property cross-plots have been diagnosed, but the degree of extrapolation along the line to find the endmembers is unknown.

In order to estimate the depth of the deep glacial Atlantic northern-southern water-mass interface, we aim to determine: 1) the magnitude of nonconservative effects on δ^{13}C, 2) plausible estimates of glacial endmembers, 3) whether recent compilations of δ^{13}C, Cd/Ca, and δ^{18}O are consistent with a steady circulation, and 4) whether one or more circulations may fit the data. As free-running models do not offer an unambiguous solution for the depth of Glacial North Atlantic Water (GNAW), we suggest that models that are explicitly constrained by observations represent a way forward [e.g., *Winguth et al.*, 2000; *Huybers et al.*, 2007]. Here we focus on the simplest model that reproduces water-mass geometries, a water-mass decomposition model [e.g., *Tomczak and Large*, 1989]. These models have been developed to simultaneously translate multiple observed seawater properties into constituent source waters [*Tomczak*, 1981; *Mackas et al.*, 1987], to handle nonconservative effects [e.g., *Karstensen and Tomczak*, 1997], and to enforce three-dimensional geometrical constraints [*Gebbie and Huybers*, 2010]. Following this approach, the source water divide is defined precisely as the isosurface with 50% of water originating from the subpolar North Atlantic surface (here defined as North Atlantic Water), and the interface thickness can be diagnosed. Defining water masses this way is natural because many tracers ultimately have their properties set by surface processes and because the surface origin provides an unambiguous basis to decompose interior ocean waters. Traditional water masses, however, are usually defined as some mixture of interior (sometimes abyssal) waters, and thus these interpretational differences must be taken into account.

In this work, we develop a model-data combination method that solves for the mass fraction of waters from all surface points on a global three-dimensional grid, that handles sparse pointwise proxy observations, and simultaneously solves the nonlinear problem for the source property values using modern-day mixing rates as a guide (Section 2). Following the introduction and the formulation of the method, we confirm that the method successfully reconstructs modern-day (Section 3) and LGM (Section 4) observations. Here we show a most plausible glacial water-mass decomposition (Section 5), as well as other solutions that satisfy the observations equally well (Section 6). A summary and outlook are included in the Conclusion (Section 7).

2. Method

The method is developed to combine information from multiple sediment core compilations (to be detailed later) and a global tracer transport model. The Total Matrix Intercomparison method [*Gebbie and Huybers*, 2010] is one such technique of this type, but that method was formulated for the modern ocean where global gridded climatologies for at least six tracers are available. In the glacial case, the endmember (or water-mass source) properties are uncertain and represent additional unknowns that create a nonlinear, non-negative total least squares problem without an obvious solution method. Therefore, the method is here extended to handle nonlinear constraints such as paleo-proxy relationships with seawater properties, as well as sparse and pointwise observations. The original two-step linearized solution method of *Gebbie and Huybers* [2010] is replaced by a streamlined one-step nonlinear optimization that does not require a parameterization of narrow bottom boundary currents nor the prescription of the mixed-layer depth (to be discussed in detail below and in the Auxiliary Material). This new reconstruction method permits the diagnosis of circulation pathways and water-mass proportions (but not rates), with global, three-dimensional maps of paleoceanographic properties produced as a side benefit. Of particular interest here is the proportion of northern and southern source waters in the deep Atlantic.

2.1. Model

Under the steady state assumption, the tracer concentration, c, results from the balance between the divergence of tracer flux and any local source, $\nabla \cdot (\vec{F}c) = q$, where $\vec{F}$ is the combined advective-diffusive mass flux of water, and q is any source (or sink). Here we enforce the steady state through a discrete form of the tracer transport equation [following *Gebbie and Huybers*, 2012]

$$c_i = \sum_{j=1}^{N} m_{ij} c_j + r q_i, \tag{1}$$

where "i" denotes a location in the ocean interior, N is the number of neighboring boxes ($N \leq 6$ in three dimensions), m_j is the fraction of water at location i that originates from box j with concentration c_j, q_i is the source of remineralized phosphate, and r is a stoichiometric ratio that makes the equation more general. Mass conservation provides the additional constraints that $\sum_{j=1}^{N} m_{ij} = 1$ and $m_{ij} \geq 0$ for all i. The net effect of advection and diffusion is contained in the m terms, where m_{ij} is the ratio of mass flux through face j to the total flux. Note that this discretized version of the tracer transport equation has the same form as a water-mass decomposition [e.g., *Tomczak and Large*, 1989] and that circulation rates do not need to be known to calculate the tracer distribution (with the tradeoff that no transients can be modeled). Rather than forming conservative tracers from nonconservative pairs [e.g., *Broecker et al.*, 1998], we retain the nonconservative source term because it adds a geometrical constraint to the problem, namely that nutrients necessarily accumulate downstream.

The model is unconventional in the sense that it is not run forward in time, nor does it include the momentum equation. An explicit model can still be formulated for each tracer:

$$\mathbf{Ac} = \mathbf{Bc}_b + \Gamma \mathbf{q}, \tag{2}$$

where $\mathbf{c}$ is the vector formed from a three-dimensional tracer distribution, $\mathbf{A}$ is the transport matrix that represents the left hand side and first right hand side term of equation (1), $\mathbf{Bc}_b$ sets the surface concentration boundary conditions (where $\mathbf{c}_b$ is a vector of sea surface values), and $\Gamma\mathbf{q}$ adds any interior sources or sinks. Given $\mathbf{A}$, $\mathbf{c}_b$, and $\mathbf{q}$ (and knowledge of $\mathbf{B}$ and Γ from the ocean geometry), one can invert for a unique global tracer distribution, $\mathbf{c}$. Mass is conserved exactly in the model, as $\mathbf{c} = 1$ is a solution to equation (2) with $\mathbf{c}_b = 1$ and $\mathbf{q} = 0$. This exact conservation is necessary to track waters from the surface to the interior without losing or gaining mass in the interior, and is in contrast with the usual approximate mass balance in inverse methods [e.g., *Wunsch*, 1978; *Mercier*, 1989; *Marchal and Curry*, 2008]. Modeling the momentum equations would add extra constraints to the problem, but at the cost of adding extra unknowns (flow speed, etc.) that are not well determined by the paleo-tracers on hand. Thus while the model is simple, such simplicity may be an advantage when focusing on the glacial water-mass problem.

The problem is solved by defining three types of unknowns: the water-mass proportions, all relevant tracer distributions on an underlying grid with $4^\circ \times 4^\circ$ horizontal resolution and 33 vertical levels, and any remineralization source for nonconservative tracers. Three types of equations, as distinguished by their mathematical form, relate the unknowns of the problem. First, equations that contain a noise term (i.e., equations with uncertainty) are used to handle sparse, pointwise observational constraints that should be satisfied within the range of their published or assumed uncertainties. Each observational constraint is determined by mapping gridded tracer values onto the observational locations, the preferable order of operations to avoid extrapolation [e.g., *Wunsch*, 1996]. Other observational constraints are also taken into account, such as the effect of the approximately 125-meter glacial sealevel drop on salinity and the oxygen-18/oxygen-16 isotope ratio of seawater (i.e., $\delta^{18}O_w$). Near conservation of the global inventory of phosphate between modern and glacial times is enforced [e.g., *Boyle*, 1992]. Second, inequality constraints such as gravitational stability and the non-negativity of tracer concentrations are also employed. Third, the tracer distributions are required to obey a steady-state circulation, as discussed above. The solution search is cast as the least-squares problem of minimizing a sum of squared model-data misfits subject to the strict enforcement of the steady-state, and is solved by the method of Lagrange multipliers [e.g., *Schlitzer*, 2007]. A complete definition of the problem and solution method are included in the Auxiliary Material.

Fitting the model to the observations can be viewed as a type of kinematic interpolation or mapping technique. Traditional methods such as optimal interpolation or objective mapping [*Bretherton et al.*, 1976; *Curry and Oppo*, 2005] can have undesirable effects when the data is sparse, such as local extrema in the estimated tracer field that are not physically sustainable in equilibrium as long as diffusion is finite [e.g., *Hide*, 1969]. For a nonconservative tracer, a tracer extremum may only exist in conjunction with an interior tracer source or sink. This steady-state assumption should be viewed as a statistical steady state, where any temporal variability that has a net diffusive or advective effect is represented by the equations used here.

3. Reference water-mass distribution

3.1. Modern-day observations

A prerequisite to estimating the glacial ocean circulation is finding a steady-state circulation that can reconstruct modern-day tracer observations. This modern-day case also serves as a reference state for comparison with the LGM. The modern-day observational datasets include δ^{13}C of dissolved inorganic carbon ($\delta^{13}C_{DIC}$) from the Global Ocean Data Analysis Project [GLODAP, *Key et al.*, 2004; *Schmittner et al.*, 2013], Carbon in Atlantic Ocean project [CARINA, *Key et al.*, 2010], and Geochemical Ocean Section Study project [GEOSECS, *Craig and Turekian*, 1980; *Kroopnick*, 1985]. The GISS $\delta^{18}O_w$ compilation is also included [*Schmidt et al.*, 1999]. Discarding observational locations that are outside the defined grid and eliminating $\delta^{18}O_w$ values less than $-8‰$ because they primarily record coastal or riverine effects, we retain 17,959 GLODAP/CARINA points, 1,974 GEOSECS points, and 22,986 GISS points, but large gaps still remain especially in the Southern Ocean (Figure 1). In the modern-day ocean, we are fortunate to have much more data for other tracers, and we apply the the gridded WOCE hydrographic climatology [*Gouretski and Koltermann*, 2004], including potential temperature, salinity, phosphate, nitrate, and oxygen, in order to fill in the gaps.

3.2. Modern-day solution

The search for a solution is started with a reasonable first guess to minimize the impact of non-linearity while signficantly influencing the final solution only in regions away from observations (see Auxiliary Material). The first guess is based on the assumption that the air-sea component of $\delta^{13}C$ (i.e., $\delta^{13}C_{as} = \delta^{13}C_{\text{DIC}} + 1.1PO_4 - 2.75$) is small. Given the gridded sea surface climatology of phosphate [*Gouretski and Koltermann*, 2004] and $\delta^{13}C_{as} = 0$, we solve for the first guess $\delta^{13}C_{\text{DIC}}$ by rearranging the definition of $\delta^{13}C_{as}$. Observations will pull $\delta^{13}C_{as}$ away from zero due to the 10-year ^{13}C air-sea equilibrium timescale [*Broecker and Peng*, 1982], invasion of aqueous CO_2 from the atmosphere [*Lynch-Stieglitz et al.*, 1995], and the temperature-dependent fractionation of ^{13}C relative to atmospheric CO_2 due to air-sea gas exchange fractionation [*Mook et al.*, 1974; *Inoue and Sugimura*, 1985]. For $\delta^{18}O_w$, the first guess is taken from the GISS gridded climatology [*Legrande and Schmidt*, 2006]. The solution characteristics and numerical stability are enhanced by the additional constraint that all surface deviations from the first guess must be large-scale (Gaussian length-scale greater than 10° longitude or latitude). The modern problem has 427,548 unknowns and requires 5,500 iterations of the search procedure before finding the successful solution detailed next (see Table 1). The fit to the WOCE climatologies of potential temperature, salinity, phosphate, nitrate, and dissolved oxygen is as good as the two-step method of *Gebbie and Huybers* [2010].

A further test of the method is whether the steady-state global distribution fits the modern-day seawater $\delta^{13}C$ data within the expected uncertainty due to measurement error, the representativeness of a steady-state in a continuously-variable and anthropogenically-contaminated ocean, and interlaboratory and sample handling variations. Although the measurement error of $\delta^{13}C_{DIC}$ is as small as 0.06‰ [*Kroopnick*, 1985], the other factors combine to yield a standard error near 0.2‰ that is roughly equal to the scatter between neighboring data points. The model fit passes a chi-squared statistical test, and here we summarize that test by analyzing the standard deviation of the misfit in two depth bins. Below 1000 meters depth, the standard deviation of the misfit (σ, top left panel, Figure 2) is an acceptable 0.14‰ (GLODAP/CARINA: 0.12‰, GEOSECS: 0.21‰). The mean misfit is less than 0.01‰ in this depth range. Above 1000 meters depth, the standard error is 0.28‰ (also top left panel, Figure 2) and the model has a systematic mean offset of 0.15‰ higher than the observations. The upper ocean misfit is consistent with the sign and magnitude expected from the Suess effect [*Suess*, 1980; *Gruber et al.*, 1996; *Olsen and Ninnemann*, 2010]. This signal of lowered oceanic $\delta^{13}C$ by the burning of fossil fuels is thus considered part of the observational noise for this study, and our result should be interpreted as a pre-industrial estimate. In summary, the remaining misfits in the upper ocean can be attributed to transient anthropogenic effects that aren't relevant to the LGM, and the deep ocean fit confirms that the model can reasonably capture $\delta^{13}C$ spatial variability, giving confidence that the method can be used for the LGM.

The seawater $\delta^{18}O_w$ misfits are assumed to be partially due to a measurement error of 0.08‰, as well as our model representation error due to seasonality and temporal variability. This variability is estimated by taking half of the published salinity uncertainty in the WOCE climatology (due to the $\delta^{18}O$-salinity relationship in *Schmidt* [1999], equation 1) as a guess of $\delta^{18}O_w$ error. Above 1000 meters depth, the model misfit averages 0.56‰, in line with the error expected due to salinity-correlated variability. The model fits the observations with a standard deviation of 0.12‰ below 1000 meters depth, which is acceptable relative to the expected 0.1-0.2‰ uncertainty derived from WOCE (top right panel, Figure 2). The successful fit to this conservative tracer in the deep ocean permits us to now move to the LGM problem.

4. LGM water-mass decomposition

4.1. LGM observations

For the Last Glacial Maximum, we select recent benthic foraminiferal compilations of $\delta^{13}C_c$ [i.e., $\delta^{13}C$ of calcite, *Hesse et al.*, 2011], Cd/Ca [*Marchitto and Broecker*, 2006], and $\delta^{18}O_c$ [*Marchal and Curry*, 2008], where these compilations include significant data from the previous works [e.g., *Sarnthein et al.*, 1994; *Curry and Oppo*, 2005]. Additional observations include 3 $\delta^{13}C_c$ observations from the Demerara Rise (D.W. Oppo & W.B. Curry, personal communication), 15 paired $\delta^{13}C_c$ and Cd/Ca measurements [*Makou et al.*, 2010], and all reported $\delta^{13}C_c$ values from *Marchitto and Broecker* [2006] that were not present in other compilations. In total, the model is constrained with 241 $\delta^{13}C_c$, 87 Cd/Ca, and 174 $\delta^{18}O_c$ observations (Figure 3). The time period of the LGM is defined to be anywhere between 24,000 to 18,000 years before present, and here we test whether an equilibrium state can describe all of the data. The accuracy of the compilations is subject to difficult issues, such as dissolution effects [*McCorkle et al.*, 1995], microhabitat effects [*Zahn et al.*, 1997; *Mackensen et al.*, 2000] and carbonate ion dependencies [*Marchitto et al.*, 2002] on Cd/Ca, and undoubtedly further refinement will occur in the future.

For the LGM, we model the additional proxy step that relates paleo records to seawater properties (see Auxiliary Material). Assumed proxy relationships are first checked by comparison of the modern-day reference tracer distributions and Late Holocene coretop values. Under the assumption that foraminifera record $\delta^{13}C_{DIC}$, the model reproduces the coretop data at the 0.24‰ standard error level. Using regression techniques to solve for the slope and intercept of the best linear relationship, differences from a slope of 1 and an intercept of 0 are statistically insignificant and we elect to use the simple model, $\delta^{13}C_c \approx \delta^{13}C_{DIC}$, for the LGM. While the standard error of the calibration is reasonable, the correlation coefficient ($r = 0.67$ between 1000 and 3500 meters depth) is lower than a historical calibration of 58 specially selected coretops [$r > 0.9$, *Duplessy et al.*, 1984]. Also, the calibration misfit has a trend of 0.2‰/5000m that increases with depth and is close to being statistically significant ($p = 0.15$). Fortunately the overall LGM vertical gradient is an order of magnitude larger than the calibration bias. Factors that contribute to error in the Late Holocene calibration include Holocene climate variability, the variable age of coretops, the difficulty in retrieving an undisturbed coretop, and low sedimentation rates in deep cores [e.g., *Oppo et al.*, 2003]. These errors, however, are expected to be smaller during the LGM, and we conclude that the Holocene coretop calibration is within an acceptable margin of error.

Cd/Ca observations are applied in terms of Cd of seawater (Cd_w), and we assume the depth-dependent calcitic partition coefficients as compiled by *Marchitto and Broecker* [2006] from previous work [*Boyle*, 1992; *Boyle et al.*, 1995]. Predictions of Cd_w at the core sites use the nonlinear relationship based on modern-day phosphate observations [*Elderfield and Rickaby*, 2000]. Modern-day coretop Cd measurements are reproduced at the 0.10 nmol/kg error level, slightly higher than the measurement error. The correlation coefficient between the model and observations, however, is not that high ($r = 0.51$) because coretops only record Cd in about half (i.e., 0.2 to 0.7nmol/kg) of its global range, giving a relatively low signal-to-noise ratio.

$\delta^{18}O_c$ is modeled as a function of seawater properties: $\delta^{18}O_c = \delta^{18}O_w - 0.21 \cdot T + 3.16$, where T is in-situ temperature and a 0.27‰ offset from seawater to calcite standards is applied [following paleotemperature equation (1), *Bemis et al.*, 1998]. Rather than modeling in-situ temperature which is subject to pressure heating effects, we model potential temperature throughout the global ocean and translate it to in-situ temperature at the core sites. To avoid grossly unrealistic distributions of temperature, we also model salinity in order to calculate the density of seawater and enforce the gravitational stability of the water column. The 192 Holocene coretop values from *Marchal and Curry* [2008] are fit with correlation coefficient of $r = 0.94$ and a standard error of 0.13‰, well within the expected error.

4.2. LGM solution

A first goal is to find any circulation that fits all of the data simultaneously. In anticipation that multiple circulations can fit the data, additional constraints are imposed in order to select the "most plausible" unique solution. For example, a reasonable remineralization profile is selected by seeking a solution with interior sources of phosphate unchanged from the modern-day (given by $\mathbf{q}$ in equation 2). Furthermore, we expect glacial $\delta^{18}O_w$ and salinity surface fields to reflect similar large-scale patterns as the modern day, but with the addition of 1.1‰ and 1.1 on the practical salinity scale, respectively, due to the 125 meters of sealevel drop [e.g., *Clark et al.*, 2009]. In accordance with the modern-day $\delta^{13}C_{as}$ values being confined to range between -0.5‰ and 0.5‰ [e.g., *Olsen and Ninnemann*, 2010], the LGM $\delta^{13}C_{as}$ values are constrained to the same range unless overruled by the observations. Adjustments to the definition of $\delta^{13}C_{as}$ are made for an assumed 4% change in glacial mean DIC and a 2‰ change in δ^{13}C fractionation [i.e., $\delta^{13}C_{as} = \delta^{13}C_{DIC} + 0.95PO_4 - 2.15$, *Broecker and Maier-Reimer*, 1992; *Lynch-Stieglitz and Fairbanks*, 1994]. A unique solution for the 344,481 unknowns of this problem is found in 700 iterations of the search algorithm (a complete list of observations and modeled tracer distributions is given in Table 2). This work primarily focuses on this most plausible LGM scenario, but the non-observational constraints imposed in this paragraph influence the solution in regions without data. Thus, the solution is non-unique in the sense that other investigators might prioritize the solution characteristics in a different way. In Section 6, we solve for other glacial solutions that fit the observations just as well, but they do not satisfy our additional preferred characteristics to the same extent.

The most plausible LGM solution reconstructs the observations at or below the expected errors. The expected δ^{13}C errors are the combined effect of the measurement error, any published replication error in multiple tests, and any uncertainty in the ability of $\delta^{13}C_c$ to represent $\delta^{13}C_{DIC}$, which totals approximately 0.15‰ throughout the water column [*Hesse et al.*, 2011]. For Cd_w, we assume that the measurement error dominates (0.08 nmol/kg), an optimistic view given the uncertainty in the modern-day Cd-phosphate global relationship [e.g., *Elderfield and Rickaby*, 2000]. For $\delta^{18}O_c$, we account for interlaboratory offsets in the measurements compiled by *Ninnemann and Charles* [2002], by subtracting 0.4‰ due to the differential treatment of samples for organic matter [*Hodell et al.*, 2003]. Uncertainty in handling these offsets is further taken into account by conservatively assuming an expected error of 0.2‰ (significantly larger than measurement error). At all depths, we find that the model error is less than or roughly equal to the expected error, with error levels of 0.12‰ in $\delta^{13}C_c$, 0.06 nmol/kg in Cd_w, and 0.13‰ in

$\delta^{18}O_c$ (bottom row, Figure 2). Due in part to the inclusion of a penalty for covarying misfits in a given depth interval (detailed in the Solution Technique section of the Auxiliary Material), the model faithfully reconstructs the increased LGM vertical range of $\delta^{13}C$ without any systematic offsets with depth (Auxiliary Figures 1-2).

The fit to the LGM data is tighter than in many recent state-of-the-art modeling studies [e.g., *Butzin et al.*, 2005; *Tagliabue et al.*, 2009; *Hesse et al.*, 2011] due to the explicit model-observation synthesis method used here. Here, the constrained solution has a model-data correlation coefficient of $r = 0.98, 0.91$, and 0.94 for $\delta^{13}C$, Cd_w, and $\delta^{18}O$, respectively (bottom row, Figure 2), in line with other rigorous statistical methods being applied to LGM general circulation models [*Dail and Wunsch*, 2013]. Correlation coefficients below about 0.9 suggest that the observations are not fit within their uncertainty, and *Huybers et al.* [2007] showed that many more scenarios could be admitted if the data constraints are weakened. One previous study found model-observation correlations that were as high as $r = 0.76$ [*Hesse et al.*, 2011] which were deemed adequate to "confirm previous reconstructions from paleoproxy records." For that model run, however, the root-mean-square model-data misfit for $\delta^{13}C$ was 0.68‰ and is not within the expected observational uncertainty. Note that the correlation of $\delta^{13}C$ with depth is $r = 0.6$. Any correlation coefficient near that level indicates that only the basic vertical structure of the LGM is captured, and thus could be considered the zero-skill level by which to judge models.

5. Comparison of modern and LGM

5.1. Distribution of Glacial North Atlantic Water

The interior advective-diffusive pathways are visualized by modeling the release of a passive dye. More specifically, dye of concentration “1” is constantly replenished at the surface of the Atlantic north of the modern-day subtropical front and removed at all other surface locations. The resulting equilibrium dye concentration is physically interpretable as the mass fraction of “northern source” or North Atlantic Water. The dye concentration, $\mathbf{g}_{north}$, is expressed as a vector, and is calculated via a boundary Green function method [*Gebbie*, 2012]. The dye paths distinguish the pathways and sources of water from the apparent water-mass distributions in seawater properties. In our LGM scenario, North Atlantic Water occupies a similar depth range as the modern ocean (Figure 4). North Atlantic Water has greater than 50% concentration at depths between 1,500 and 4,000 meters for both modern and LGM cases. The total volume of the glacial Atlantic below 1000m is 41% northern source versus 43% southern source water, where southern waters are defined to originate from south of the southern subtropical front. This LGM volumetric census is basically unchanged (north: 41%, south: 45%). Southern-source water during the LGM (not shown) occupies the intermediate and bottom depths and sandwiches North Atlantic Water much as it does today. The eastern Atlantic is similarly unchanged between the LGM and modern-day (see Auxiliary Figure 12). Independent carbonate ion evidence also suggests that northern-source waters did not shoal as much as previously interpreted from δ^{13}C compilations [*Yu et al.*, 2008].

5.2. Low δ^{13}C in the Glacial North Atlantic

The inferred modern-day $\delta^{13}C_{DIC}$ is generally similar to the GEOSECS-based reconstruction [*Kroopnick*, 1985], but with spatial noise reduction by our steady-state circulation method. The 0.8 $\delta^{13}C_{DIC}$ contour tracks the propagation of NADW in the western Atlantic (top panel, Figure 5), extending southward to 40°S between 1500 and 4000 meters depth. Tropical and subtropical $\delta^{13}C_{DIC}$ is relatively unchanged between the LGM and modern-day, consistent with the Bahamas $\delta^{13}C_c$ values as high as 1.6‰ between 400 to 1500m [*Slowey and Curry*, 1995] (bottom panel, Figure 5). Large glacial-to-modern differences, however, exist in the abyssal South Atlantic where glacial $\delta^{13}C_{DIC}$ is as low as -0.9‰. Disregarding the tropical intermediate ocean, the reconstruction of this work is similar to that of *Curry and Oppo* [2005], including the path of the +0.8‰ contour that outcrops near 45°S, deepens with a slight indication of a northward incursion of Antarctic Intermediate Water, and eventually descends to approximately 2000 meters in the North Atlantic. Many of the apparent model-data misfits are due to the zonal distance required to map onto the meridional section, and disappear when the comparison is made at the right longitude (Auxiliary Figures 3-4). Overall, the modeled tracers corroborate previous mappings in the deep ocean including the shoaling of deep δ^{13}C and Cd_w isosurfaces, and there appears to be no major contradiction with previously inferred distributions. An atlas of δ^{13}C, Cd_w, and $\delta^{18}O_c$ for western and eastern Atlantic sections (Auxiliary Figures 8-12) shows that the shoaling occurs in the eastern basin as well, although there is some zonal structure that we will not attempt to explain here.

If δ^{13}C is assumed to be unaffected by biological effects and we follow previous estimates of the northern and southern water-mass δ^{13}C values [e.g., north: 1.5‰, south: -0.2 to -0.9‰, *Curry and Oppo*, 2005], the 50-50 mixture of the two water masses would be given by an isocontour between 0.3‰ and 0.65‰. These contours appear to originate in the Southern Ocean and descend to 2500 to 3000 meters depth in the North Atlantic. The 50% northern source contour diagnosed above, however, is deeper than 4000 meters depth. Thus, the low $\delta^{13}C$ values in the mid-depth North Atlantic do not match the GNAW concentration contours previously calculated, and the assumption of $\delta^{13}C$ as a nonconservative tracer in the deep ocean must be revisited.

5.3. Effects of remineralization

Despite nutrients being preferentially remineralized in the upper ocean (central panels, Figure 6), more remineralized nutrients accumulate in the deep glacial ocean than the modern-day (left panels, Figure 6). Waters decrease their $\delta^{13}C$ at a rate of 0.95‰/(μmol/kg) as remineralized phosphate is added, giving a total $\delta^{13}C$ drop as large as 0.8‰. The significance of this effect is seen in the preformed $\delta^{13}C$ field, defined here to be $\delta^{13}C$ distribution resulting from the same surface boundary values but without remineralization (right panels, Figure 6). The 0.6‰ preformed-$\delta^{13}C$ contour descends from the Southern Ocean to 4000 meters depth rather than 3000 meters, in better agreement with the diagnosed extent of GNAW. The continued existence of northern-source water with increased nutrient content has been argued previously in the eastern Atlantic [*Sarnthein et al.*, 1994] and the South Pacific [*Matsumoto and Lynch-Stieglitz*, 1999]. In our scenario, the utilization of the deep ocean to store nutrients may be a clue that the Atlantic hoarded excess carbon from the atmosphere during glacial times [e.g., *Boyle*, 1988].

Remineralized nutrients are typically expected to be found at intermediate depths where the input of remineralized material, given by the product of the remineralization rate and the residence time in a model gridbox, is maximized. The accumulation of more than 0.8 μmol/kg remineralized phosphate in modern intermediate waters follows this expectation. The intermediate-depth maximum occurs because the residence time increases with depth below the surface more rapidly than the remineralization rate decreases. For the LGM, some nutrients accumulate at depths greater than their initial source of remineralization due to ocean transport and aging. Here, remineralized phosphate is decomposed into northern and southern sources based upon the water mass to which the phosphate was originally added (see the Appendix for a detailed definition and derivation). The deep maximum of remineralized phosphate near 3000 meters depth is identified with the transport of GNAW and is a key difference to the modern-day (left panels, Figure 7). Lower GNAW accumulates nutrients in the Nordic Seas, descends over the deep overflows, and then accumulates additional nutrients on its southward journey. These waters originate with δ^{13}C values between 0.6 and 1.0‰ and then eventually obtain values between 0.3‰ and 0.6‰ and occupy the Atlantic below 2000 meters depth. With its lowered δ^{13}C values, Lower GNAW can masquerade as southern source water.

Lower GNAW is inferred to have low δ^{13}C values and high amounts of remineralized phosphate, similar to the northern-source water modeled by *Kwon et al.* [2012]. In that study, the northern-source water follows a counterintuitive pathway with northward spreading into the deep Atlantic. To determine the direction of spreading of our modeled GNAW, we note that the model requires the monotonic increase of nutrients downstream, which we use as a diagnostic here. If the northern source of remineralized phosphate, calculated above, is normalized by the concentration of northern source water, then any water-mass mixing effect is eliminated and we are left with a GNAW-specific remineralized phosphate concentration (right panels, Figure 7, see Appendix for derivation). In the North Atlantic, the normalized remineralization always increases southward, suggesting a more conventional north-to-south path of GNAW. Furthermore, GNAW accumulates much less phosphate above 2500 meters depth than it does below. Note that this diagnostic gives the largest values in the Southern Ocean, but because the mass concentration of GNAW is low there, the effect on the total remineralized phosphate is small. If the remineralization rate is spatially uniform, as might be a good approximation below 1000 meters depth [e.g., *Marchal and Curry*, 2008], then the normalized remineralization pattern would be identical to an ideal age map with an unknown scaling factor. Under this assumption, the model indicates that GNAW may fill much of the Atlantic, but the rate of filling is much slower below 2500m depth, consistent with the vertical structure of radiocarbon in the western Atlantic [e.g., *Keigwin*, 2004].

A dye released in the mid-depth South Atlantic (1000m to 3000m depth, 30°S to 40°S) indicates that the fate of North Atlantic Water was altered during the LGM (Figure 8). The Southern Ocean plays a major role in the closure of the meridional overturning circulation [e.g., *Marshall and Speer*, 2012], and here we diagnose a shift in the dividing line of the overtuning cells relative to the water-mass core of North Atlantic Water. The proportion of water that continues to the lower Antarctic Bottom Water (AABW) overturning cell is increased during the LGM at the expense of the upper Antarctic Intermediate Water (AAIW) cell [e.g., *Toggweiler et al.*, 2006]. This routing of water ensures that bottom waters also have more remineralized nutrients during the LGM than the modern-day. A number of mechanistic questions remain, such as determining the extent to which subsurface diabatic processes or surface adiabatic processes close the circulation.

5.4. Air-sea signature of δ^{13}C

The 0‰ contour of the nearly conservative tracer, $\delta^{13}C_{as}$, is a good marker of the divide between northern and southern source waters in the modern-day ocean. AAIW values are as high as 0.7‰ due in part to enhanced wind-driven ventilation [*Oppo and Fairbanks*, 1987; *Broecker and Maier-Reimer*, 1992; *Charles et al.*, 1993], and AABW values are also positive (0.1-0.3‰) due to isotopic equilibrium effects at low temperature [*Mook et al.*, 1974]. NADW values, on the other hand, are lowered to -0.5‰ due to northward flowing subtropical waters and atmospheric invasion of CO_2 (top panel, Figure 9). The modeled LGM $\delta^{13}C_{as}$ values don't give such a clear picture. AABW has a $\delta^{13}C_{as}$ value lower than -0.5‰, but AAIW is slightly positive in accord with previous works [*Oppo and Horowitz*, 2000; *Makou et al.*, 2010]. GNAW is reconstructed to have $\delta^{13}C_{as}$ of 0‰-0.2‰, which is a less distinct signal than the 0.5‰ inferred by *Marchitto and Broecker* [2006]. Those strongly positive values are restricted to the shallow subtropical waters and eastern Atlantic in the model. Consequently the 0‰ isocontour no longer offers a clear delineation between northern and southern glacial source waters. Observational errors in δ^{13}C and Cd combine to yield an approximate 0.3‰ error on $\delta^{13}C_{as}$, and 60% of all data points are not significantly different from zero. Thus, it is difficult to constrain the model to have nonzero glacial $\delta^{13}C_{as}$ values. Without a distinct water-mass signature, the datasets used here offer no barrier to GNAW having $\delta^{13}C_{as}$ near 0‰ and occupying similar depths as the modern case.

Increased sea ice and poor ventilation have been suggested to answer the conundrum of why LGM $\delta^{13}C_{as}$ is so much lower in glacial AABW than the modern [e.g., *Lynch-Stieglitz and Fairbanks*, 1994; *Marchitto and Broecker*, 2006]. Such processes would isolate waters but not create the extreme $\delta^{13}C_{as}$, however. Explicit modeling of air-sea exchange is not carried out in this work, but a number of possible explanations for the conundrum emerge here. In additional experiments where $\delta^{13}C_{as}$ is constrained more strongly to be close to 0‰, we find that the data require AABW values at least as low as -0.5‰, and thus our most plausible LGM solution may have $\delta^{13}C_{as}$ that is lower than required. Furthermore, a large mismatch between the coretop Cd and modern-day PO_4 observations exists, suggesting that additional processes may be recorded by the Cd/Ca proxy. Another possibility is that the assumed phosphate-δ^{13}C stoichiometry used in the definition of $\delta^{13}C_{as}$ is not correct. We find that the both the modern-day and LGM PO_4-δ^{13}C relationships are predominantly linear, but that the slope is steeper than expected for the LGM (-1.3 ‰/μmol/kg, Auxiliary Figure 5). If a steeper slope could be rationalized as being due to biologic effects, $\delta^{13}C_{as}$ for glacial AABW would be much smaller.

5.5. The Mid-Depth Glacial Property Gradient

The mid-depth maximum of δ^{13}C in the Brazil Margin set of cores shoaled from 2500m to 1500m at the LGM and provided a key piece of evidence for shoaled GNAW [e.g., *Curry and Oppo*, 2005]. Here we fill in the gaps between the observational locations by averaging the model over the Brazil Margin region (55° to 40°W, 24° to 32°S). Note that the model-data misfit in the upper 1000 meters of the modern δ^{13}C is due to the Suess effect, with the magnitude of the effect consistent with *Olsen and Ninnemann* [2010] (leftmost panel, Figure 10). The modeled mid-depth δ^{13}C maximum shoals to 1800 meters depth at the LGM relative to 2400 meters for the modern-day. The modeled minimum in LGM Cd_w is nearly co-located with the mid-depth δ^{13}C maximum, and it is 700 meters shallower in the LGM (second panel, Figure 10). Modeled LGM $\delta^{18}O_c$ reconstructs the vertical gradient near 1800m depth, but the magnitude

(6×10^{-4} ‰/m) is about 40% smaller than that identified by *Lund et al.* [2011] (third panel, Figure 10). The model is faithful to the vertical structure of the observations, as there are no systematic model offsets at any depth (Auxiliary Figure 2), and suggesting that the discrepancy is statistically insignificant. Inclusion of a potential vorticity tracer in the model would potentially better constrain the stratification and these vertical gradients. In addition, the model reproduces a glacial $\delta^{18}O_c$ distribution that is higher at the Brazil Margin than the Blake Outer Ridge at all depths, as diagnosed in the observations [*Curry and Oppo*, 2005].

The model permits the vertical structure of North Atlantic Water to be diagnosed at the Brazil Margin, including the depth of the maximum water-mass concentration [i.e., the water-mass "core," *Wüst*, 1935]. Using the 50% mass fraction to judge the extent of the water mass, the North Atlantic Water thickness is basically unchanged (modern: 1800m, LGM: 1600m), as previously seen in the meridional sections. Previous observational interpretations seem to be picking up the shoaling of the water-mass core from the modern 2500m to 1750m during the LGM (rightmost panel, Figure 10), although this is still somewhat smaller than 1000 meters. The shoaling of the water-mass core, however, does not imply that the interface of North Atlantic Water and Antarctic Bottom Water also shoaled by a similar amount. The model indicates that vertical gradient below the water-mass core reflects the beginning of mixing zone between northern and southern waters, but the 50-50 mixture occurs much deeper in the water column.

6. Other Glacial Solutions

The water-mass decomposition of this work shows that the extent of North Atlantic Water was slightly altered during the LGM, and here we investigate the sensitivity of that result to the non-observational assumptions. A first test is determining whether the glacial water-mass distribution must differ at all from the modern-day. Inverse methods first developed for the modern ocean [e.g. *Wunsch*, 1978; *Mercier*, 1989] have been used to show that δ^{13}C observations, even when combined with oxygen-isotope information, could not constrain the LGM Atlantic overturning circulation to be different than the modern-day circulation [*Legrand and Wunsch*, 1995], although they treated δ^{13}C as conservative. The addition of radiocarbon with realistic error estimates did not remedy this lack of power in the data [*Huybers et al.*, 2007]. Here, we perform a second inversion that seeks surface boundary conditions to fit the LGM data while keeping the circulation pathways fixed to the modern-day. Although the standard deviation of the misfit between the reconstructed tracer fields and LGM observations can be made small, the surface boundary conditions in the Weddell Sea are required to have δ^{13}C values of -2‰ and $\delta^{13}C_{as}$ values less than -1‰, both of which are outside the range of present observations. Therefore water-mass changes in the LGM are statistically significant, even if they are not as large as previously interpreted.

In our main LGM inversion, AABW has a δ^{13}C value lower than -0.8‰ and $\delta^{18}O_c$ higher than 5.0‰, and here we investigate the sensitivity of the northern-southern water-mass interface to those endmembers. For this purpose, we perform a third LGM inversion where the global δ^{13}C distribution is enforced to be no lower than -0.2‰, effectively setting the AABW endmember to that value. This LGM scenario features a reasonable western Atlantic δ^{13}C distribution and a northern-southern source interface that shoals to 3000 meters depth with an increased southern-water influence in the deep Atlantic (Figure 11). This circulation does not require AABW $\delta^{18}O_c$ to be greater than 5.0‰. The δ^{13}C observations that are lower than -0.2‰, however, are not fit within their uncertainty unless microhabitat effects are invoked. Further constraints on Southern Ocean $\delta^{18}O_c$, as might be obtained by better understanding the salinity and seawater $\delta^{18}O$ of glacial AABW, may help determine whether this third LGM scenario is realistic.

Two sample diagnostics illustrate the dependence of GNAW extent on the AABW endmember. The region over which northern source waters constitute the majority of waters by mass is outlined by the 0.5 mass fraction (or 50%) isosurface (Figure 12). The main LGM inversion of Section 4 and the inversion with $\delta^{13}C > -0.2‰$ represent limiting cases for the deep water-mass interface. While the deep water-mass interface is sensitive to the AABW endmember, the water-mass core of GNAW shoals near the Brazil Margin and Blake Outer Ridge observations in both inversions. We suggest that these well-observed profiles represent a strong local constraint on the circulation, but that these data points do not evenly influence all of the Atlantic.

We infer an increased accumulation of nutrients in the deep Atlantic in our main inversion, and here we investigate whether this is required by the LGM observations. For this purpose, we perform a fourth LGM inversion where the effect of remineralization on $\delta^{13}C$ and Cd is set to zero ($r = 0$ in equation 1). Surprisingly, an LGM scenario with no remineralization can still fit the LGM observations while producing a reasonable western Atlantic $\delta^{13}C$ distribution. This fourth LGM scenario features a northern-southern source interface that is intermediate to the two limiting cases in the previous paragraph. Thus, the combination of LGM observations and the simple tracer transport model only weakly constrain the total amount of remineralization in the glacial Atlantic. This scenario, however, requires surface $\delta^{13}C_{as}$ values to be twice as large as the modern ocean, and therefore is unlikely to reflect the true LGM.

7. Conclusion

To determine the depth of Glacial North Atlantic Water, a water mass decomposition method is developed that accounts for sparse, pointwise observations, the limited information regarding surface and water-mass endmember properties, and the indirect measurement of seawater properties through proxy data types. The solution method is aided by additional constraints, such as the gravitational stability of the water column, the conservation of the global inventory of phosphate, accounting for lowered sealevel on salinity and seawater δ^{18}O, and using the modern ocean as a template where glacial data are not available. Combining recent compilations of δ^{13}C, Cd/Ca, and δ^{18}O with the statistical method that accounts for observational errors, we find that the datasets are self-consistent within reasonably assumed error bounds, that a steady-state circulation can explain the data as well as should be expected, and that the sandwiching of deep northern-source water between southern-sourced intermediate and bottom waters need not change during the Last Glacial Maximum. In this LGM scenario, the water-mass core of GNAW shoals by nearly 1000 meters, but GNAW dominates the Atlantic over a similar vertical range as does modern-day NADW. Although other scenarios can also fit the data, our most plausible solution for the glacial circulation suggests that the current generation of paleo-proxy observations do not require the renaming of NADW to GNAIW.

Even though the most-plausible glacial circulation of mass grossly resembles the modern, nutrients accumulate in much greater amounts in the deep glacial Atlantic. In particular, Lower GNAW accumulates nutrients more efficiently than Upper GNAW, consistent with an increase in the residence time of deep Atlantic waters. If nutrients accumulate in the deep glacial Atlantic in concentrations as great as the modern Pacific as suggested by our LGM solution, this would represent an important piece in understanding glacial CO_2 drawdown.

In much of the path of modern-day North Atlantic Deep Water, glacial $\delta^{13}C_{as}$ is not significantly different from zero, and therefore Glacial North Atlantic Water can have roughly the same extent as today's NADW. Although strongly positive $\delta^{13}C_{as}$ values have been inferred for the North Atlantic in previous works, such values are not required due to the lack of observations in the western and northern Atlantic, the combined errors from $\delta^{13}C$ and Cd in forming the water-mass tracer, and the difficulty in distinguishing the northern-source endmember from the subtropical one. Another major uncertainty is due to the sensitivity of the deep water-mass interface to the glacial AABW endmember for $\delta^{13}C$ and $\delta^{18}O_c$. A model that explicitly includes the additional air-sea and ice-sea interactions of the Southern Ocean promises to better constrain these difficult-to-observe quantities.

Appendix A: Accumulation of remineralized phosphate

The amount of phosphate that has accumulated due to remineralization, $\mathbf{p}_r$, is calculated by solving equation (2): $\mathbf{p}_r = \mathbf{A}^{-1}\Gamma\mathbf{q}$, where $\mathbf{p}_r$ replaces the generic tracer, $\mathbf{c}$, and $\mathbf{c}_b = 0$ in equation (2) because no nutrients have accumulated at the surface by definition. The remineralized phosphate is equivalently defined as: $\mathbf{p}_r = \mathbf{p} - \mathbf{p}^*$, the difference between the actual phosphate distribution, $\mathbf{p}$, and the preformed phosphate distribution, $\mathbf{p}^*$ [*Gruber and Sarmiento*, 2002]. The remineralized phosphate can also be decomposed according to the water mass in which the phosphate was originally added. As remineralized phosphate is added uniformly to each gridbox, we identify the amount of phosphate added to a particular water mass, $\mathbf{p}_g$ (units of μmol/[kg seawater]), as the product of the source in a gridbox ($\mathbf{q}$ in equation 2), and the fraction of water belonging to that water mass, $\mathbf{g}$. Thus, $\mathbf{p}_g = \mathbf{A}^{-1}\Gamma(\mathbf{q} \circ \mathbf{g})$, where $\circ$ represents element-by-element multiplication (or the Schur product) of two vectors. The sum of $\mathbf{p}_g$ for all water masses is equal to the total remineralized phosphate, $\mathbf{p}_r$. To track the monotonic increase of remineralized nutrients downstream in a water mass, $\mathbf{p}_g$ is scaled by the mass of the water mass of interest, rather than the total mass of seawater. Thus, the normalized concentration of remineralized phosphate in a water mass is: $\hat{\mathbf{p}}_g = [\mathbf{A}^{-1}\Gamma(\mathbf{q} \circ \mathbf{g})] \oslash \mathbf{g}$, where $\oslash$ is element-by-element division and the units are μmol/[kg of water mass]. If τ, the residence time of each grid box, replaces $\mathbf{q}$ in the previous equation, then $\hat{\mathbf{p}}_g$ becomes $\mathbf{a}_g$, the ideal or mean age of that water mass [following *Gebbie and Huybers*, 2012].

Acknowledgments.

I thank W.B. Curry, D.W. Oppo, and A. Schmittner for graciously providing data before its publication, M. Schmidt for his minFunc MATLAB optimization toolbox, O. Marchal, D.W. Oppo, D. Thornalley, and C. Wunsch for comments on the manuscript, and K.-F. Huang and F. Primeau for helpful discussions. GG is supported by NSF grants OIA-1124880 and OCE-1301907, and the WHOI Ocean and Climate Change Institute.

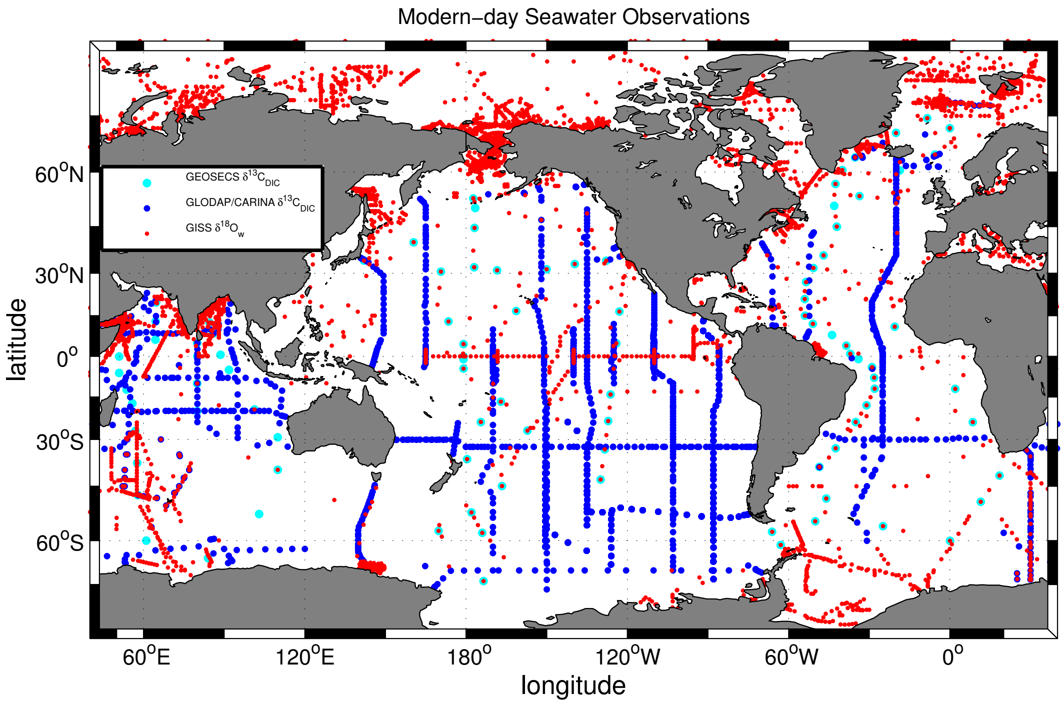

Figure 1. Modern-day seawater measurements of $\delta^{13}C_{DIC}$ from GEOSECS (*cyan points*) and GLODAP/CARINA (*blue points*), as well as $\delta^{18}O_w$ from GISS (*red points*).

Modeled tracers	r	C_0	reference
$\delta^{13}C_{DIC}$ [‰VPDB]	-1.1	$\delta^{13}C_{as} = 0$	*Broecker and Maier-Reimer* [1992]
$\delta^{18}O_w$ [‰VSMOW]	0	climatology	*Legrande and Schmidt* [2006]
$PO_4 [\mu mol/kg]$	1	climatology	*Gouretski and Koltermann* [2004]
$NO_3 [\mu mol/kg]$	15.5	climatology	*Gouretski and Koltermann* [2004]
$O_2 [\mu mol/kg]$	-170	climatology	*Gouretski and Koltermann* [2004]
θ [°C]	0	climatology	*Gouretski and Koltermann* [2004]
Salinity [ ]	0	climatology	*Gouretski and Koltermann* [2004]
Total Unknowns		427,548	
Observations	**Uncertainty**	**# points**	**reference**
GLODAP $\delta^{13}C_{DIC}$ [‰VPDB]	0.2 (deep), 0.8 (shallow)	17,959	*Key et al.* [2004, 2010]; *Schmittner et al.* [2013]
GEOSECS $\delta^{13}C_{DIC}$ [‰VPDB]	0.4 (deep), 1.2 (shallow)	1,974	*Kroopnick* [1985]
$\delta^{18}O_w$ [‰VSMOW]	0.08, 0.40, 5.79 ‰	22,986	*Schmidt et al.* [1999]
$PO_4 [\mu mol/kg]$	0.004, 0.25, 5.02	74,064	*Gouretski and Koltermann* [2004]
$NO_3 [\mu mol/kg]$	0.11, 1.80, 13.04	74,064	*Gouretski and Koltermann* [2004]
$O_2 [\mu mol/kg]$	0.8, 20.0, 85.6	74,064	*Gouretski and Koltermann* [2004]
θ [°C]	0.002, 0.62, 6.18	74,064	*Gouretski and Koltermann* [2004]
Salinity [ ]	0.0003, 0.10, 7.20	74,064	*Gouretski and Koltermann* [2004]
Total Obs		413,239	

Table 1. Summary of the modern-day problem. The model-specific parameters are the 1) the type of gridded field, 2) r, the stoichiometric ratio, and 3) C_o, the first guess surface field in the solution method. The observation-specific parameters include 1) the observational type, 2) the minimum, median, and maximum uncertainty (where one number is given if all quantities are the same), 3) the number of data points, and 4) the data reference.

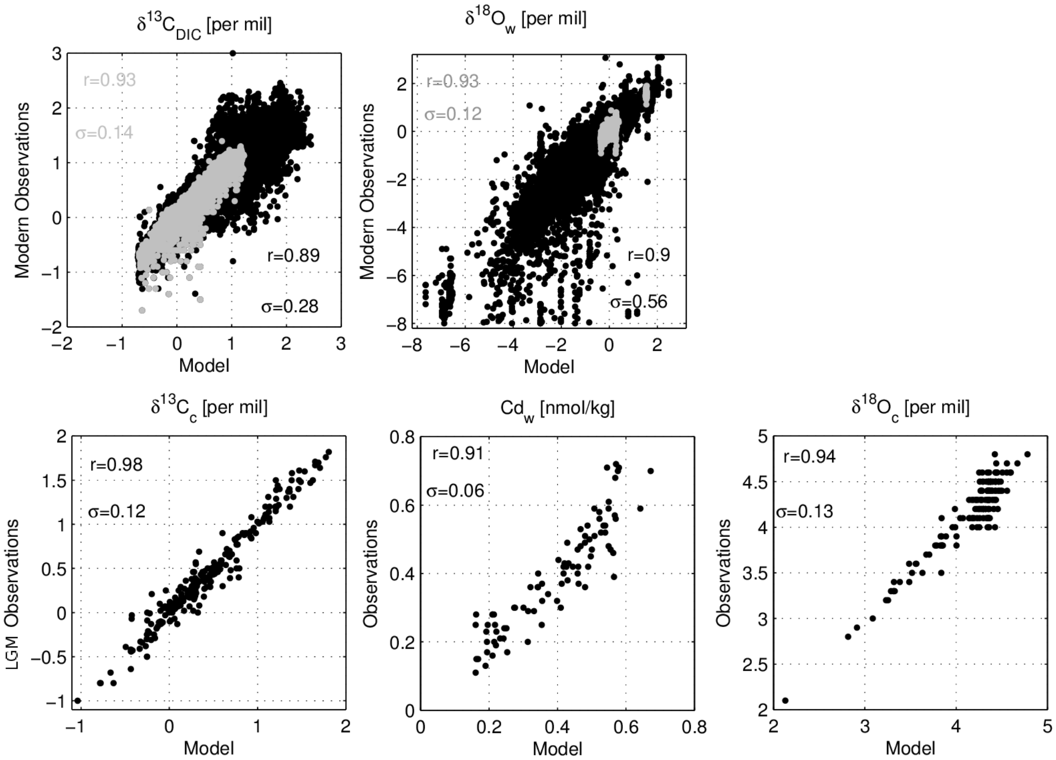

Figure 2. *Top row*: Scatter plots of modern-day seawater observations (*ordinate*) versus modeled values at the observational sites (*abscissa*) for $\delta^{13}C_{DIC}$ (*left*), and $\delta^{18}O_w$ (*right*). The observations are are separated into those above (*black*) and below (*gray*) 1000 meters depth. The correlation coefficient, r, and standard error, σ, are given for the two cases. *Bottom row*: Similar to top row, but for LGM values of $\delta^{13}C_c$ (*left*), Cd_w (*middle*), and $\delta^{18}O_c$. No distinction is made for the depth of the observations.

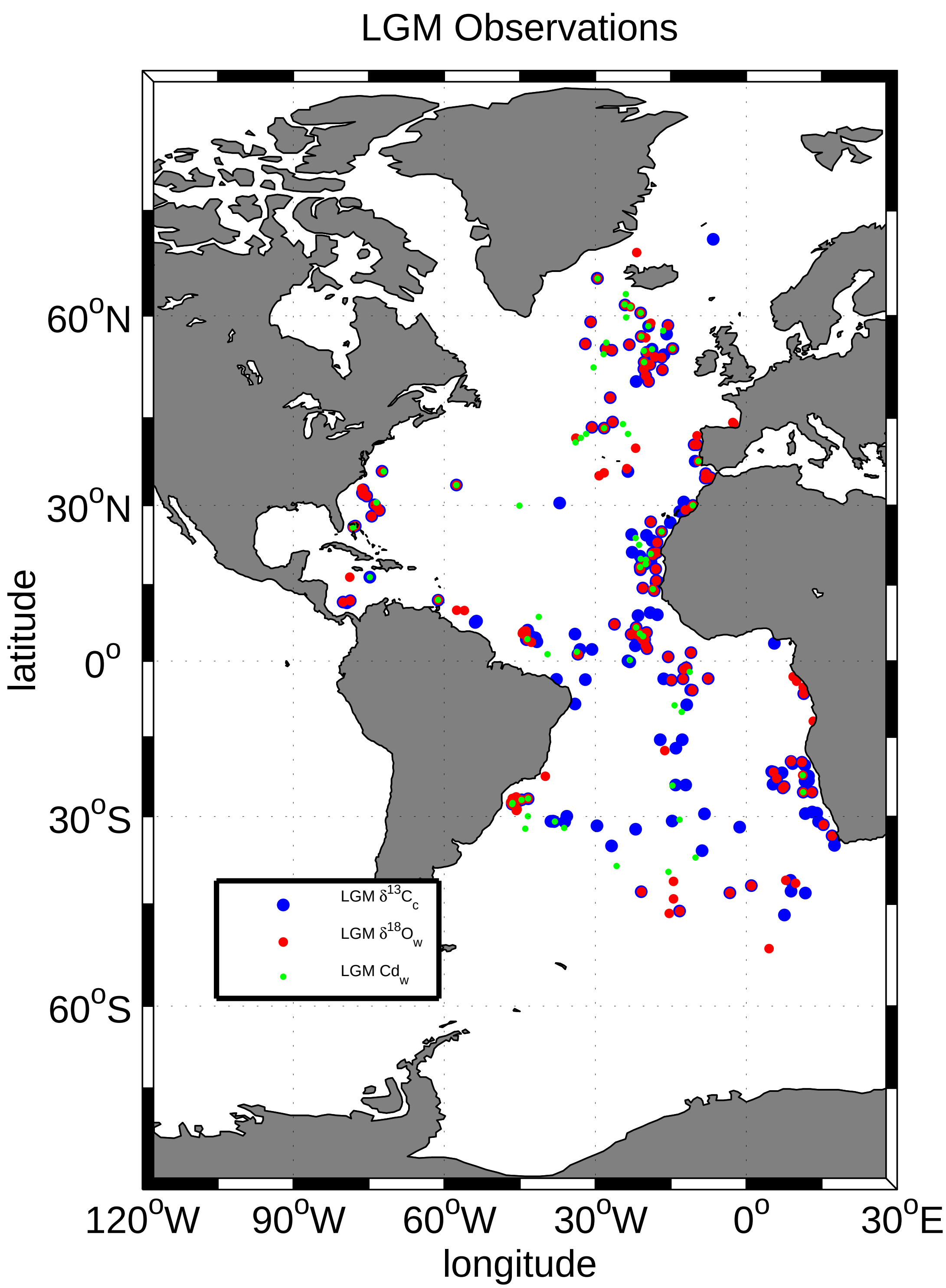

Figure 3. Last Glacial Maximum observations from benthic foraminifera: δ^{13}C (*blue*), δ^{18}O (*red*), and Cd$_w$ (*green*).

Modeled tracers	r	C_0	reference
$\delta^{13}C_{\text{DIC}}$ [‰VPDB]	-0.95	$\delta^{13}C_{as} = 0$	*Broecker and Maier-Reimer* [1992]
$\delta^{18}O_w$ [‰VSMOW]	0	modern + 1.1‰	*Legrande and Schmidt* [2006]
$PO_4[\mu mol/kg]$	1	modern	*Gouretski and Koltermann* [2004]
θ [°C]	0	MARGO SST	*Kucera et al.* [2006]; *Waelbroeck et al.* [2009]
Salinity [ ]	0	1.0326× modern	*Gouretski and Koltermann* [2004]
Total Unknowns		344,481	
Observations	**Uncertainty**	**# points**	**reference**
$\delta^{13}C_c$ [‰VPDB]	0.08, 0.13, 0.32	241	*Hesse et al.* [2011], *Marchitto and Broecker* [2006]; *Makou et al.* [2010]
$\delta^{18}O_c$ [‰VSMOW]	0.2	174	*Marchal and Curry* [2008]
Cd_w [nmol/kg]	0.08	87	*Marchitto and Broecker* [2006]; *Makou et al.* [2010]
Mean Salinity [ ]	0.2	1	sealevel change, *Clark et al.* [2009]
Mean $\delta^{18}O$ [‰]	0.3	1	sealevel change, *Clark et al.* [2009]
Mean PO_4 [μmol/kg]	0.1	1	modern inventory, *Boyle* [1992]
Total Obs		490	

Table 2. Summary of the Last Glacial Maximum problem. The model-specific parameters are the 1) the type of gridded field, 2) r, the stoichiometric ratio, and 3) C_o, the first guess surface field in the solution method. The observation-specific parameters include 1) the observational type, 2) the minimum, median, and maximum uncertainty, 3) the number of data points, and 4) the data reference (*column 4*).

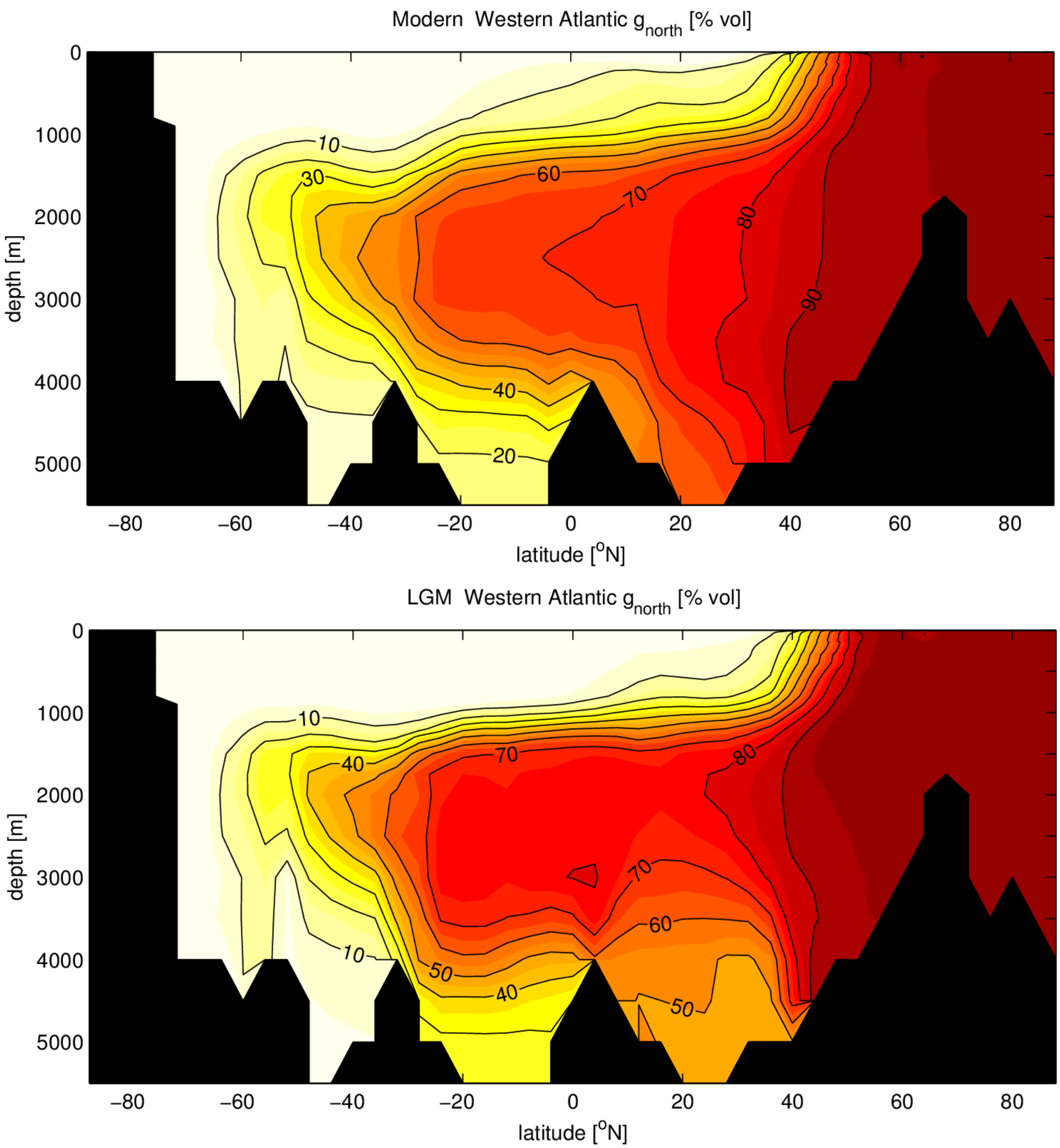

Figure 4. Percentage of North Atlantic Water by volume for the modern (*top panel*) and LGM (*bottom panel*) cases. The contour interval is 10% as calculated by multiplying the mass fraction (i.e., $\mathbf{g}_{north}$) by 100.

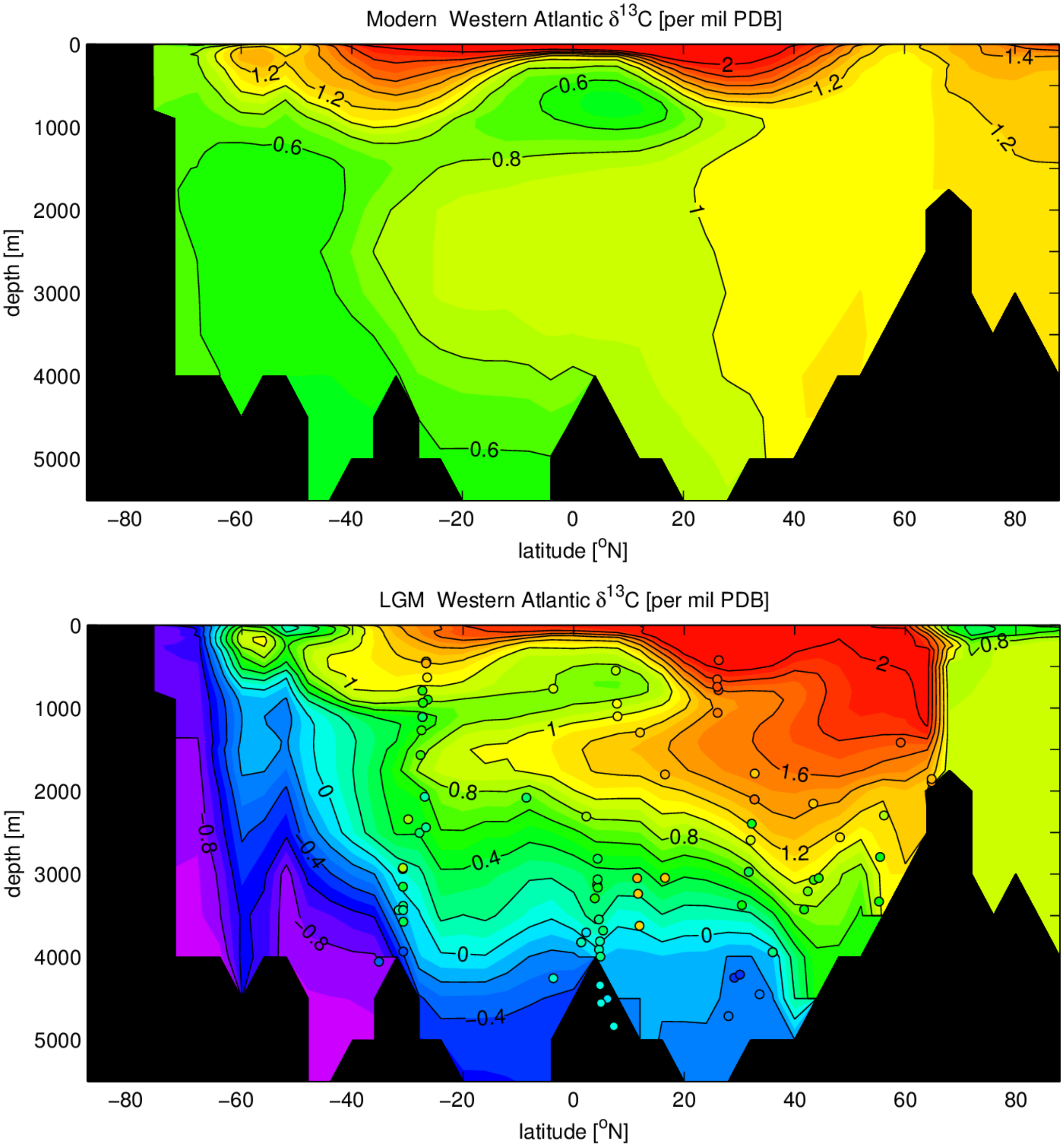

Figure 5. Western Atlantic $\delta^{13}C_{DIC}$ from the modern-day (*top*) and the Last Glacial Maximum (*bottom*). $\delta^{13}C_c$ observations from the Atlantic west of 35°W (*colored circles*) are included on the same colorscale as the model (*bottom panel*). GLODAP, CARINA, and GEOSECS points used to reconstruct the modern field are suppressed for clarity in the top panel. The section is constructed along the Western Atlantic GEOSECS cruise track.

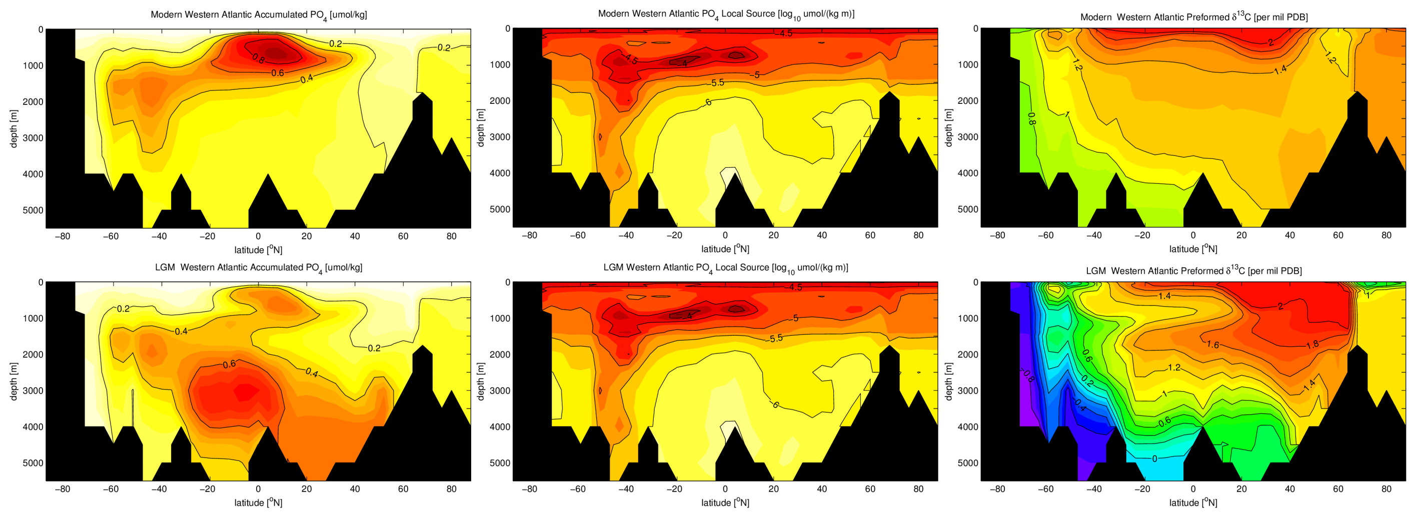

Figure 6. Comparison of modern (*top row*) and LGM (*bottom row*) reconstructions of accumulated phosphate (*left column*), base-10 logarithm of local remineralized phosphate source (*middle column*), and preformed δ^{13}C (i.e., δ^{13}C*, *right column*).

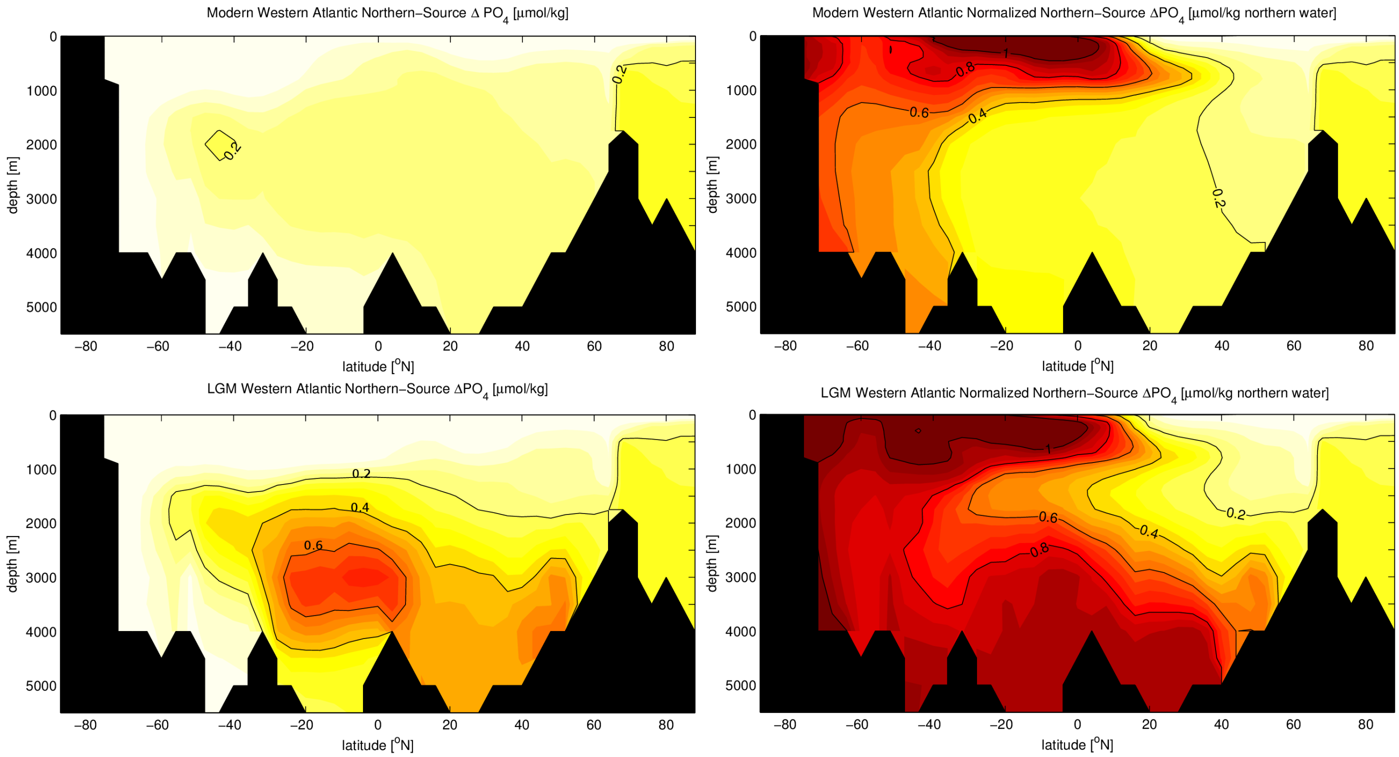

Figure 7. Comparison of modern (*top row*) and LGM (*bottom row*) contribution of remineralized phosphate by GNAW ($\mathbf{p}_{north}$ in the text, *left column*), and the contribution normalized by the mass of GNAW ($\hat{\mathbf{p}}_{north}$, *right column*).

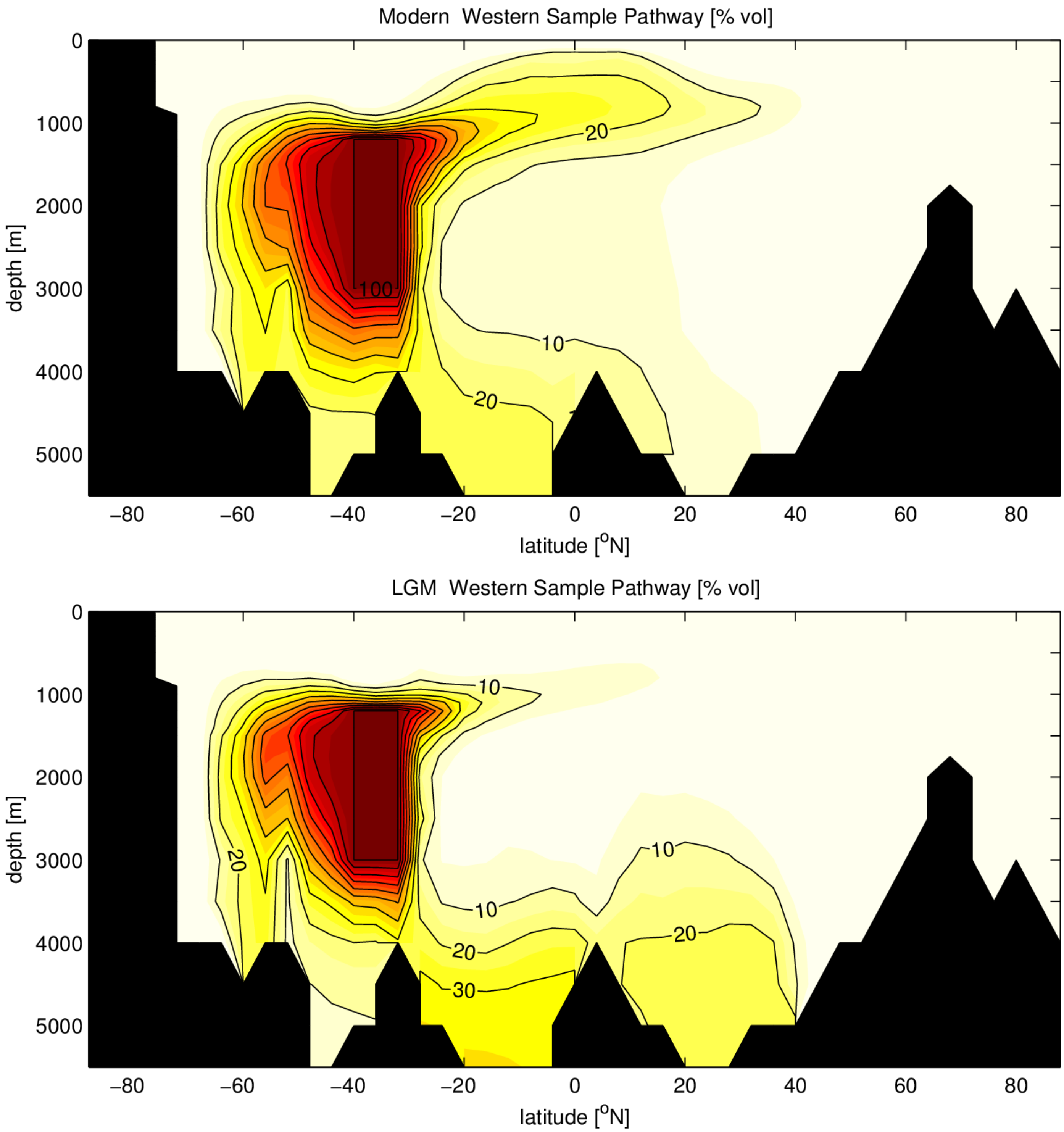

Figure 8. Percentage of water that last transited a mid-depth southern ocean box on its path from the surface (*top*: modern-day, *bottom*: LGM).

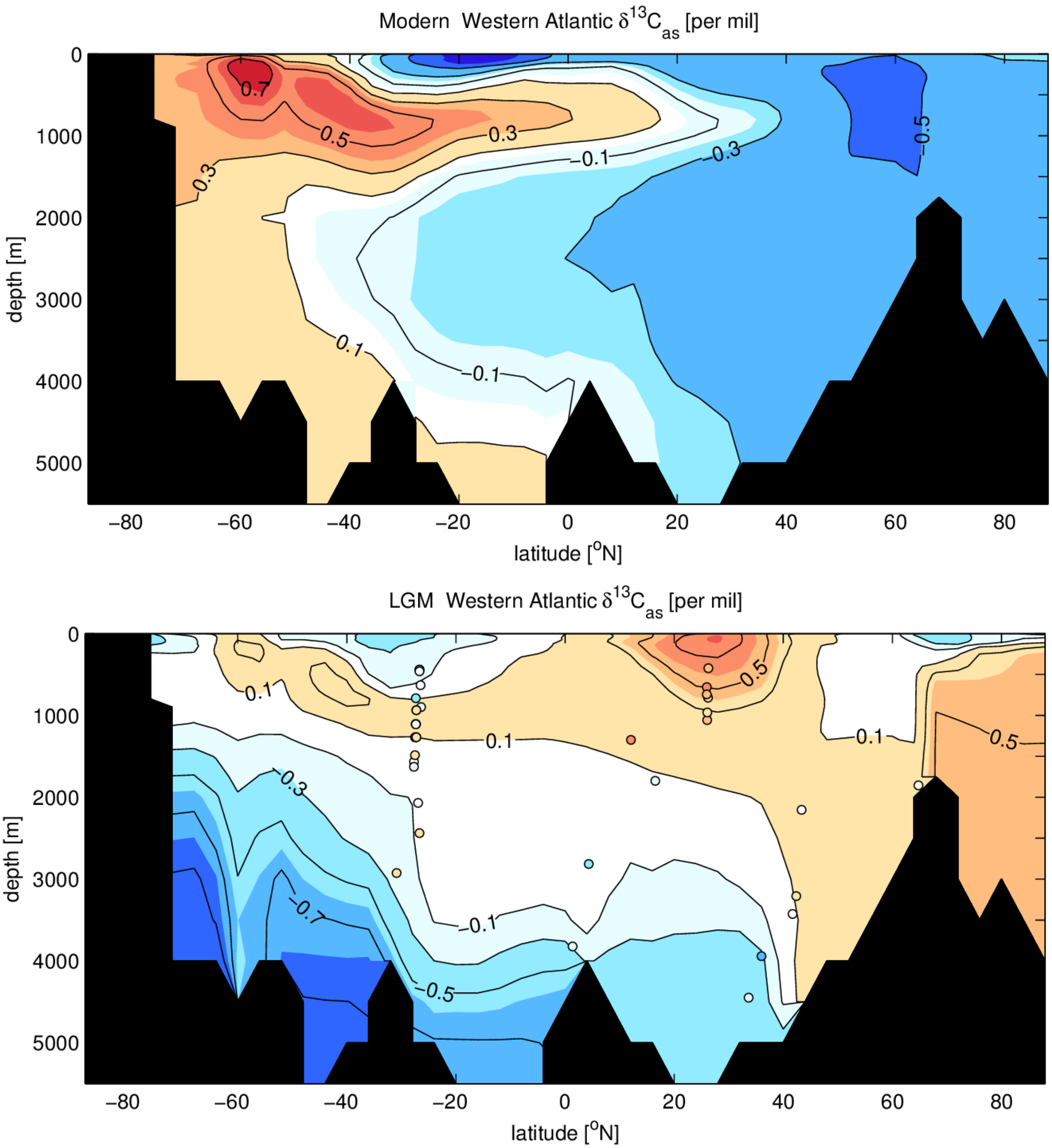

Figure 9. Same as Figure 5, but for $\delta^{13}C_{as}$. Observations of $\delta^{13}C_{as}$ are diagnosed at locations where Cd_w and $\delta^{13}C_c$ are both available.

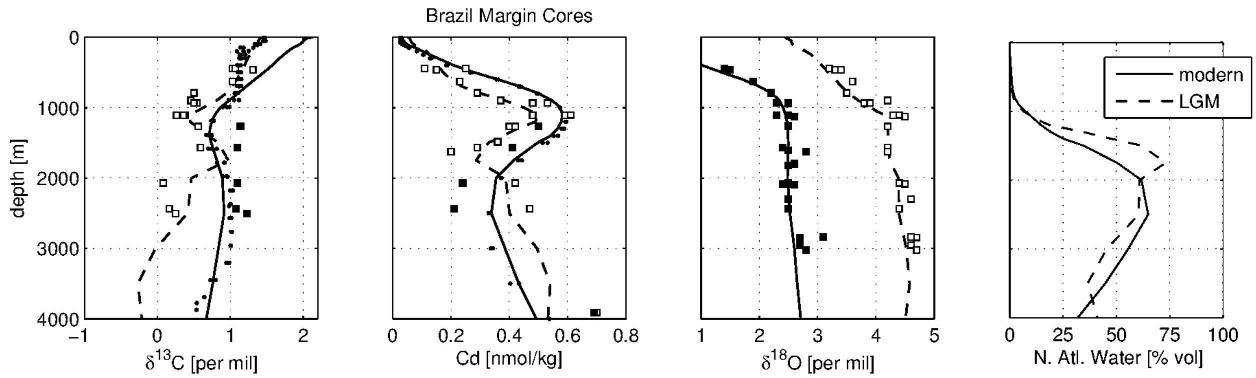

Figure 10. Brazil Margin δ^{13}C (*leftmost panel*), Cd (*second panel from left*), $\delta^{18}O_c$ (*third panel*), and North Atlantic Water concentration ($\mathbf{g}_{north}$, *rightmost panel*). Modern-day seawater observations (*black points*), Late Holocene observations (*closed squares*), glacial observations (*open squares*), and the modern (*solid line*) and glacial modeled profiles (*dashed line*) are included.

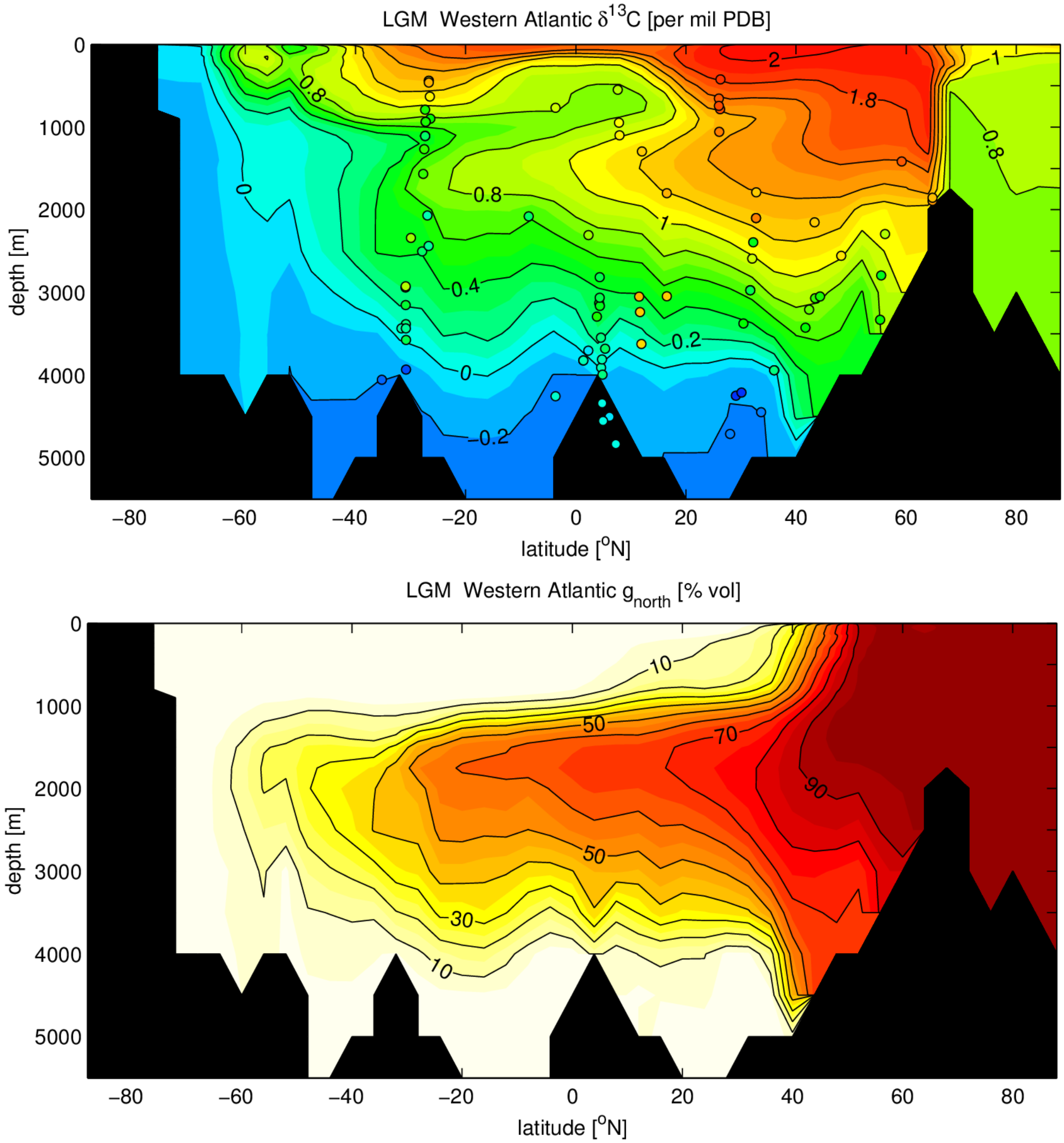

Figure 11. Western Atlantic latitude-depth section of δ^{13}C (*top panel*) and percentage of northern-source water ($100 \times \mathbf{g}_{north}$, *bottom panel*) in an alternative LGM scenario with $\delta^{13}C > -0.2$‰. Colored circles represent LGM δ^{13}C observations west of 35°W.

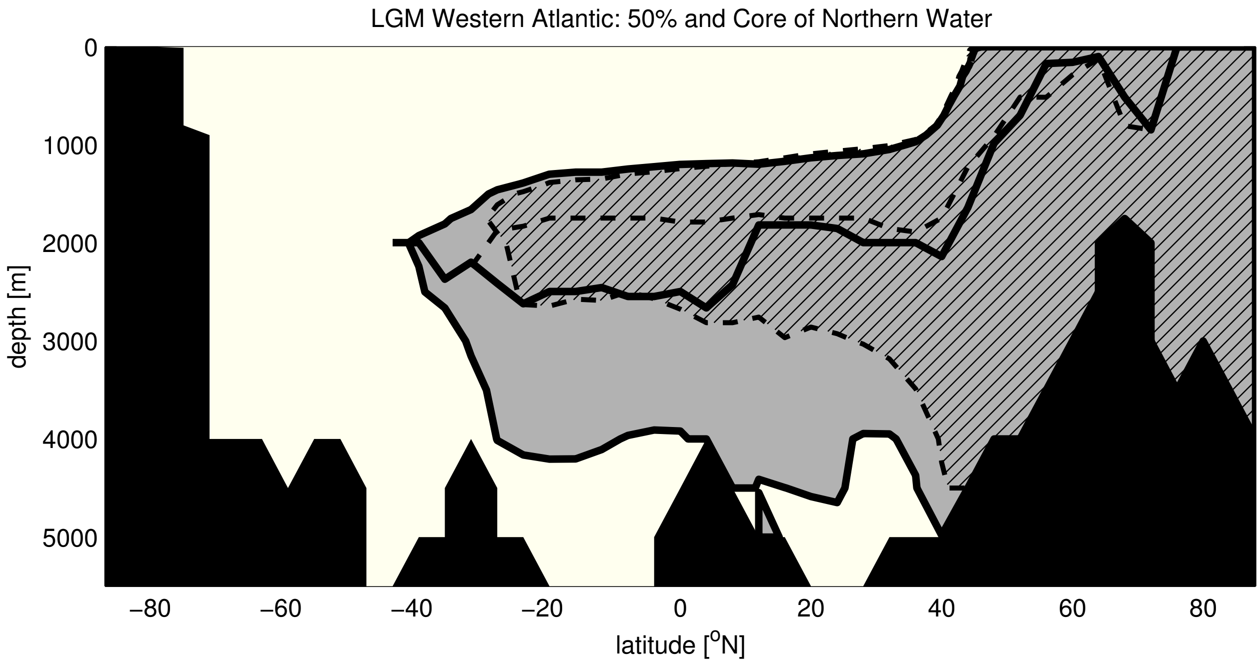

Figure 12. The extent of GNAW in the western Atlantic given by the 50% concentration line for the main LGM inversion (*gray with solid outline*), and the alternative LGM inversion that had no δ^{13}C values below -0.2‰ (*hatched with dashed outline*). The water-mass core of GNAW is also denoted with the same line type as the respective 50% GNAW contour.

References

Bemis, B., H. Spero, J. Bijma, and D. Lea (1998), Reevaluation of the oxygen isotopic composition of planktonic foraminifera: Experimental results and revised paleotemperature equations, *Paleoceanography*, *13*(2), 150–160.

Boyd, P., and T. Trull (2007), Understanding the export of biogenic particles in oceanic waters: Is there consensus?, *Progress in Oceanography*, *72*(4), 276 – 312, doi: http://dx.doi.org/10.1016/j.pocean.2006.10.007.

Boyle, E. (1988), Cadmium: Chemical tracer of deepwater paleoceanography, *Paleoceanography*, *3*(4), 471–489.

Boyle, E., and L. Keigwin (1982), Deep circulation of the North Atlantic over the last 200,000 years: Geochemical evidence, *Science*, *218*(4574), 784.

Boyle, E. A. (1992), Cadmium and delta13C paleochemical ocean distributions during the Stage 2 Glacial Maximum, *Annual Review of Earth and Planetary Sciences*, *20*(1), 245–287.

Boyle, E. A., and L. Keigwin (1987), North Atlantic thermohaline circulation during the past 20,000 years linked to high-latitude surface temperature, *Nature*, *330*, 35–40.

Boyle, E. A., L. Labeyrie, and J.-C. Duplessy (1995), Calcitic foraminiferal data confirmed by cadmium in aragonitic hoeglundina: Application to the Last Glacial Maximum in the northern Indian Ocean, *Paleoceanography*, *10*(5), 881–900.

Bretherton, F., R. Davis, and C. Fandry (1976), A technique for objective analysis and design of oceanographic experiments applied to MODE-73, *Deep-Sea Res*, *23*, 559–582.

Broecker, W., and E. Maier-Reimer (1992), The influence of air and sea exchange on the carbon isotope distribution in the sea, *Global Biogeochemical Cycles*, *6*(3), 315–320.

Broecker, W. S., and T. H. Peng (1982), *Tracers in the sea*, Lamont-Doherty Earth Observatory of Columbia University.

Broecker, W. S., et al. (1998), How much deep water is formed in the Southern Ocean?, *Journal of Geophysical Research-oceans*, *103*(C8), 15,833–15,843.

Butzin, M., M. Prange, and G. Lohmann (2005), Radiocarbon simulations for the glacial ocean: the effects of wind stress, Southern Ocean sea ice and Heinrich events, *Earth and Planetary Science Letters*, *235*(1), 45–61.

Charles, C., J. Wright, and R. Fairbanks (1993), Thermodynamic influences on the marine carbon isotope record, *Paleoceanography*, *8*(6), 691–697.

Clark, P., A. Dyke, J. Shakun, A. Carlson, J. Clark, B. Wohlfarth, J. Mitrovica, S. Hostetler, and A. McCabe (2009), The last glacial maximum, *Science*, *325*(5941), 710–714.

Craig, H., and K. K. Turekian (1980), The GEOSECS program - 1976-1979, *Earth Plan. Sci. Lett.*, *49*(2), 263–265.

Curry, W., and G. Lohmann (1982), Carbon isotopic changes in benthic foraminifera from the western South Atlantic: Reconstruction of glacial abyssal circulation patterns., *Quaternary Research*, *18*(2), 218–235.

Curry, W., and D. Oppo (2005), Glacial water mass geometry and the distribution of $\delta^{13}C$ of $\sum CO_2$ in the Western Atlantic Ocean, *Paleoceanography*, *20*, 10.1029/2004PA001,021.

Curry, W., J. Duplessy, L. Labeyrie, and N. Shackleton (1988), Changes in the distribution of δ13C of deep water ∑CO2 between the last glaciation and the Holocene, *Paleoceanography*, *3*(3).

Dail, H., and C. Wunsch (2013), Dynamical reconstruction of upper ocean conditions in the Last Glacial Maximum Atlantic, submitted.

Duplessy, J., N. Shackleton, R. Matthews, W. Prell, W. Ruddiman, M. Caralp, and C. Hendy (1984), ^{13}C record of benthic foraminifera in the last interglacial ocean: Implications for the carbon cycle and the global deep water circulation, *Quaternary Research*, *21*(2), 225–243.

Duplessy, J., N. Shackleton, R. Fairbanks, L. Labeyrie, D. Oppo, and N. Kallel (1988), Deepwater source variations during the last climatic cycle and their impact on the global deepwater circulation, *Paleoceanography*, *3*(3).

Elderfield, H., and R. Rickaby (2000), Oceanic Cd/P ratio and nutrient utilization in the glacial Southern Ocean, *Nature*, *405*(6784), 305–310.

Gebbie, G. (2012), Tracer transport timescales and the observed Atlantic-Pacific lag in the timing of the last Termination, *Paleoceanography*, *27*, PA3225, doi:10.1029/2011PA002,273.

Gebbie, G., and P. Huybers (2010), Total matrix intercomparison: a method for resolving the geometry of water-mass pathways, *J. Phys. Oceanogr.*, *40*(8), 1710–1728, DOI: 10.1175/2010JPO4272.1.

Gebbie, G., and P. Huybers (2012), The mean age of ocean waters inferred from radiocarbon observations: sensitivity to surface sources and accounting for mixing histories, *J. Phys. Oceanogr.*, *42 (2), DOI: 10.1175/JPO-D-11-043.1*, 291–305.

Gouretski, V., and K. Koltermann (2004), WOCE Global Hydrographic Climatology, *Tech. Rep. 35*, Berichte des Bundesamtes für Seeschifffahrt und Hydrographie.

Gruber, N., and J. L. Sarmiento (2002), Large-scale biogeochemical-physical interactions in elemental cycles, *The sea*, *12*, 337–99.

Gruber, N., J. L. Sarmiento, and T. F. Stocker (1996), An improved method for detecting anthropogenic CO2 in the oceans, *Global Biogeochemical Cycles*, *10*(4), 809–837.

Hesse, T., M. Butzin, T. Bickert, and G. Lohmann (2011), A model-data comparison of δ^{13}C in the glacial Atlantic Ocean, *Paleoceanography, 26, PA3220.*, *26*, PA3220.

Hide, R. (1969), Dynamics of the atmospheres of the major planets with an appendix on the viscous boundary layer at the rigid bounding surface of an electrically-conducting rotating fluid in the presence of a magnetic field, *J. Atmos. Sci.*, *26*, 841–853.

Hodell, D. A., C. D. Charles, J. H. Curtis, P. G. Mortyn, U. S. Ninnemann, and K. A. Venz (2003), Data report: Oxygen isotope stratigraphy of ODP Leg 177 sites 1088, 1089, 1090, 1093, and 1094, pp. 1–26.

Huybers, P., G. Gebbie, and O. Marchal (2007), Can paleoceanographic tracers constrain meridional circulation rates?, *J. Phys. Oceanogr.*, *37*(2), 394–407, dOI: 10.1175/JPO3018.1.

Inoue, H., and Y. Sugimura (1985), Carbon isotopic fractionation during the CO2 exchange process between air and sea water under equilibrium and kinetic conditions, *Geochimica et Cosmochimica Acta*, *49*, 2453–2460.

Johnson, D. A. (1982), Abyssal teleconnections: Interactive dynamics of the deep ocean circulation, *Palaeogeogr. Palaeoclmatol. Palaeoecol.*, *38*(12), 93–128.

Karstensen, J., and M. Tomczak (1997), Ventilation processes and water mass ages in the thermocline of the southeast Indian Ocean, *Geophysical Research Letters*, *24*(22), 2777–2780.

Keigwin, L. D. (2004), Radiocarbon and stable isotope constraints on last glacial maximum and younger dryas ventilation in the western north atlantic, *Paleoceanography*, *19*(4).

Key, R. M., et al. (2004), A global ocean carbon climatology: Results from Global Data Analysis Project (GLODAP), *Global Biogeochemical Cycles*, *18*(4).

Key, R. M., et al. (2010), The CARINA data synthesis project: introduction and overview, *Earth System Science Data*, *2*, 105–121.

Kroopnick, P. (1985), The distribution of C-13 of SIGMA-CO2 in the world oceans, *Deep-Sea Res. Part A*, *32*(1), 57–84.

Kucera, M., A. Rosell-Mele, R. Schneider, C. Waelbroeck, and M. Weinelte (2006), Multiproxy approach for the reconstruction of the glacial ocean surface (MARGO), *Quaternary Science*

Reviews, *24*.

Kwon, E. Y., M. P. Hain, D. M. Sigman, E. D. Galbraith, J. L. Sarmiento, and J. Toggweiler (2012), North Atlantic ventilation of ”southern-sourced” deep water in the glacial ocean, *Paleoceanography*, *27*(2), PA2208.

Legrand, P., and C. Wunsch (1995), Constraints from paleotracer data on the North-Atlantic circulation during the last glacial maximum, *Paleoceanography*, *10*, 1011–1045.

Legrande, A. N., and G. A. Schmidt (2006), Global gridded data set of the oxygen isotopic composition in seawater, *Geophysical Research Letters*, *33*(12).

Lund, D., J. Adkins, and R. Ferrari (2011), Abyssal atlantic circulation during the last glacial maximum: Constraining the ratio between transport and vertical mixing, *Paleoceanography*, *26*(26), 1213.

Lynch-Stieglitz, J. (2003), Tracers of past ocean circulation, *Treatise on Geochemistry*, *6*, 433–451.

Lynch-Stieglitz, J., and R. G. Fairbanks (1994), A conservative tracer for glacial ocean circulation from carbon isotope and palaeo-nutrient measurements in benthic foraminifera, *Nature*, *369*, 308–310.

Lynch-Stieglitz, J., T. Stocker, W. Broecker, and R. Fairbanks (1995), The influence of air-sea exchange on the isotopic composition of oceanic carbon: Observations and modeling, *Global Biogeochemical Cycles*, *9*(4), 653–665.

Lynch-Stieglitz, J., W. Curry, and N. Slowey (1999), Weaker Gulf Stream in the Florida Straits during the Last Glacial Maximum, *Nature*, *402*, 644–648.

Lynch-Stieglitz, J., et al. (2007), Atlantic Meridional Overturning Circulation during the Last Glacial Maximum, *Science*, *316*(5821), 66–69.

Mackas, D. L., K. L. Denman, and A. F. Bennett (1987), Least-squares multiple tracer analysis of water mass composition, *Journal of Geophysical Research*, *92*(C3), 2907–2918.

Mackensen, A., S. Schumacher, J. Radke, and D. Schmidt (2000), Microhabitat preferences and stable carbon isotopes of endobenthic foraminifera: clue to quantitative reconstruction of oceanic new production?, *Marine Micropaleontology*, *40*(3), 233–258.

Makou, M. C., D. W. Oppo, and W. B. Curry (2010), South Atlantic intermediate water mass geometry for the last glacial maximum from foraminiferal Cd/Ca, *Paleoceanography*, *25*(4).

Marchal, O., and W. Curry (2008), On the abyssal circulation in the glacial Atlantic, *Journal of Physical Oceanography*, *38*(9), 2014–2037.

Marchitto, T., and W. Broecker (2006), Deep water mass geometry in the glacial Atlantic Ocean: A review of constraints from the paleonutrient proxy Cd/Ca, *Geochemistry Geophysics Geosystems*, *7*(12), Q12,003.

Marchitto, T. M., D. W. Oppo, and W. B. Curry (2002), Paired benthic foraminiferal Cd/Ca and Zn/Ca evidence for a greatly increased presence of Southern Ocean Water in the glacial North Atlantic, *Paleoceanography*, *17*(3), 10–18.

Marshall, J., and K. Speer (2012), Closure of the meridional overturning circulation through Southern Ocean upwelling, *Nature Geoscience*.

Martin, J. H., G. A. Knauer, D. M. Karl, and W. W. Broenkow (1987), Vertex: Carbon cycling in the northeast pacific, *Deep Sea Research A. Oceanographic Research Papers*, *34*(2), 267–285.

Matsumoto, K., and J. Lynch-Stieglitz (1999), Similar glacial and Holocene deep water circulation inferred from Southeast Pacific benthic foraminiferal carbon isotope composition, *Paleoceanography*, *14*(2), 149–163.

McCorkle, D. C., P. A. Martin, D. W. Lea, and G. P. Klinkhammer (1995), Evidence of a dissolution effect on benthic foraminiferal shell chemistry: d13C, Cd/Ca, Ba/Ca, and Sr/Ca results from the Ontong Java Plateau, *Paleoceanography*, *10*(4), 699–714.

Mercier, H. (1989), A study of the time averaged circulation in the western North Atlantic by simultaneous nonlinear inversion of hydrographic and current meter data, *DSR*, *36*, 297–313.

Mook, W., J. Bommerson, and W. Staverman (1974), Carbon isotope fractionation between dissolved bicarbonate and gaseous carbon dioxide, *Earth and Planetary Science Letters*, *22*, 169.

Ninnemann, U. S., and C. D. Charles (2002), Changes in the mode of southern ocean circulation over the last glacial cycle revealed by foraminiferal stable isotopic variability, *201*(2), 383–396.

Olsen, A., and U. Ninnemann (2010), Large δ13C gradients in the preindustrial north atlantic revealed, *Science*, *330*(6004), 658.

Oppo, D. W., and R. G. Fairbanks (1987), Variability in the deep and intermediate water circulation of the atlantic ocean during the past 25,000 years: Northern hemisphere modulation of the southern ocean, *Earth and Planetary Science Letters*, *86*(1), 1–15.

Oppo, D. W., and M. Horowitz (2000), Glacial deep water geometry: South Atlantic benthic foraminiferal Cd/Ca and d13C evidence, *Paleoceanography*, *15*(2), 147–160.

Oppo, D. W., and S. J. Lehman (1993), Mid-Depth Circulation of the Subpolar North Atlantic during the Last Glacial Maximum, *Science*, *259*(5098), 1148–1152.

Oppo, D. W., J. F. McManus, and J. L. Cullen (2003), Palaeo-oceanography: Deepwater variability in the Holocene epoch, *Nature*, *422*(6929), 277–277.

Ostermann, D. R., and W. B. Curry (2000), Calibration of stable isotopic data: An enriched δ^{18}O standard used for source gas mixing detection and correction, *Paleoceanography*, *15*(3), 353–360.

Sarnthein, M., K. Winn, S. J. A. Jung, J.-C. Duplessy, L. Labeyrie, H. Erlenkeuser, and G. Gansen (1994), Changes in East Atlantic deep water circulation over the last 30,000 years: Eight time silce reconstructions, *Paleoceanography*, *9*, 209–267.

Schlitzer, R. (2007), Assimilation of radiocarbon and chlorofluorocarbon data to constrain deep and bottom water transports in the world ocean, *Journal of Physical Oceanography*, *37*(2), 259–276.

Schmidt, G., G. Bigg, and E. Rohling (1999), Global seawater oxygen-18 database - v1.21, http://data.giss.nasa.gov/o18data.

Schmidt, G. A. (1999), Error analysis of paleosalinity calculations, *Paleoceanography*, *14*(3), 422–429.

Schmittner, A., N. Gruber, A. C. Mix, R. M. Key, A. Tagliabue, and T. K. Westberry (2013), Biology and air-sea gas exchange controls on the distribution of carbon isotope ratios (δ^{13}C) in the ocean, *Biogeosciences Discussions*, *10*(5), 8415–8466, doi:10.5194/bgd-10-8415-2013.

Slowey, N., and W. Curry (1995), Glacial-interglacial differences in circulation and carbon cycling within the upper western North Atlantic, *Paleoceanography*, *10*(4), 715–732.

Streeter, S. S., and N. J. Shackleton (1979), Paleocirculation of the deep North Atlantic: 150,000-year record of benthic foraminifera and oxygen-18, *Science*, *203*(4376), 168–171.

Suess, E. (1980), Particulate organic carbon flux in the oceans-surface and oxygen utilization, *Nature*, *288*, 260–262.

Tagliabue, A., L. Bopp, D. Roche, N. Bouttes, J. Dutay, R. Alkama, M. Kageyama, E. Michel, and D. Paillard (2009), Quantifying the roles of ocean circulation and biogeochemistry in governing ocean carbon-13 and atmospheric carbon dioxide at the last glacial maximum, *Clim. Past*, *5*, 695–706.

Toggweiler, J., J. Russell, and S. Carson (2006), Midlatitude westerlies, atmospheric co2, and climate change during the ice ages, *Paleoceanography*, *21*(2), 1–A2005.

Tomczak, M. (1981), A multi-parameter extension of temperature/salinity diagram techniques for the analysis of non-isopycnal mixing, *Progress in Oceanography*, *10*(3), 147–171.

Tomczak, M., and D. G. B. Large (1989), Optimum multiparameter analysis of mixing in the thermocline of the eastern Indian Ocean, *Journal of Geophysical Research-oceans*, *94*(C11), 16,141–16,149.

Waelbroeck, C., et al. (2009), Constraints on the magnitude and patterns of ocean cooling at the last glacial maximum, *Nature Geoscience*, *2*(2), 127–132.

Weber, S., et al. (2007), The modern and glacial overturning circulation in the Atlantic ocean in PMIP coupled model simulations, *Climate of the Past*, *3*(1), 51–64.

Winguth, A., D. Archer, E. Maier-Reimer, and U. Mikolajewicz (2000), Paleonutrient data analysis of the glacial Atlantic using an adjoint ocean general circulation model, in *Inverse Methods in Global Biogeochemical Cycles*, edited by P. Kasibhatla, M. Heimann, D. Harley, N. Mahowald, R. Prinn, and P. Rainer, pp. 171–183, AGU Geophysical Monograph Series.

Wunsch, C. (1978), The general circulation of the North Atlantic west of 50°W determined from inverse methods, *Rev. Geophys.*, *16*, 583–620.

Wunsch, C. (1996), *The Ocean Circulation Inverse Problem*, 437 pp., Cambridge University Press.

Wüst, G. (1935), Schichtung und zirkulation des Atlantischen Ozeans. Die stratosphare., in *Wissenschaftliche Ergebnisse der Deutschen Atlantischen Expedition auf dem Forschungs-und Vermessungsschiff "Meteor" 1925-1927 (reprinted as "The Stratosphere of the Atlantic Ocean")*, edited by W. J. Emery, pp. 1–180.

Yu, J., H. Elderfield, and A. M. Piotrowski (2008), Seawater carbonate ion-δ^{13}c systematics and application to glacial–interglacial north atlantic ocean circulation, *Earth and Planetary Science Letters*, *271*(1), 209–220.

Zahn, R., J. Schönfeld, H.-R. Kudrass, M.-H. Park, H. Erlenkeuser, and P. Grootes (1997), Thermohaline instability in the north atlantic during meltwater events: Stable isotope and ice-rafted detritus records from Core SO75-26KL, Portuguese Margin, *Paleoceanography*, *12*(5), 696–710.